Coastal and inland water pixels extraction algorithm (WiPE) from spectral shape analysis and HSV transformation applied to Landsat 8 OLI and Sentinel-2 MSI

Dat Dinh Ngoc, Hubert Loisel, Cédric Jamet, Vincent Vantrepotte, Lucile Duforêt-Gaurier, Chung Doan Minh, Antoine Mangin

Coastal and inland water pixels extraction algorithm (WiPE) from spectral shape analysis and HSV transformation applied to Landsat 8 OLI and Sentinel-2 MSI

Dat Dinh Ngoc[1, 2, 3], Hubert Loisel[2, 3, *], Cédric Jamet[2,3], Vincent Vantrepotte[2, 3], Lucile Duforêt-Gaurier[3], Chung Doan Minh[1], Antoine Mangin[4]

[1]Space Technology Institute, Vietnam Academy of Science and Technology, 18 Hoang Quoc Viet, Cau Giay, Hanoi, Vietnam; dndat@sti.vast.vn, dmchung@sti.vast.vn

[2]LOTUS, University of Science and Technology of Hanoi, 18 Hoang Quoc Viet, Cau Giay, Hanoi, Vietnam; cedric.jamet@ univ-littoral.fr

[3]Laboratoire d'Océanologie et de Géosciences, Université du Littoral-Côte-d'Opale, Université Lille, CNRS, UMR 8187, LOG, 32 avenue Foch, Wimereux, France ; vincent.vantrepotte@ univ-littoral.fr, lucile.duforet@ univ-littoral.fr

[4]ACRI-ST, 06904 Sophia Antipolis Cedex, France; antoine.mangin@acri.fr

[*]Correspondence: hubert.loisel@univ-littoral.fr; Tel: +33-321-99-6420

Abstract: Identification of water pixels over natural water bodies is a prerequisite step prior to applying algorithms dedicated to the estimation of bio-optical properties of surface waters from remote sensing observations. For visible remote sensing sensors, clouds affect the quantity and quality of the observations, directly by hiding part of the scene and indirectly by their shadows. A certain level of confusion could occur for detection of clouds over turbid (i.e. bright) waters and for detection of their shadows over any kind of surface water. Some algorithms exist but their performance is not satisfactory, especially over turbid waters where cloud-free pixels are sometimes classified as cloud or land, leading to a loss of data. This is particularly important for medium spatial resolution observations such as those performed by the Operational Land Imager (OLI) sensor on Landsat-8 or the Multispectral Instrument (MSI) on Sentinel-2 (a and b). In the frame of this study, we developed a two-step algorithm for the

extraction of water pixels (referred to as WiPE) for these medium spatial resolution sensors. In contrast to other approaches based on the top of atmosphere (TOA) reflectance, this algorithm uses the Rayleigh-corrected TOA reflectance ($\rho_{rc}(\lambda)$) as input parameter allowing the spectral signature of each object to be better characterized. The first step, based on the $\rho_{rc}(\lambda)$ spectral shape analysis of each object, allows water pixels to be discriminated from cloud, vegetation, barren land, and constructions pixels. The second step, in which the $\rho_{rc}(\lambda)$ spectra are transferred into the Hue-Saturation-Value space, greatly improves the detection of cloud shadow over waters. This second step, based on the processing of the whole image, does not require any knowledge on the location and altitude of clouds. Thin clouds are identified during the two steps of the algorithm. This algorithm has been successfully tested over a broad range of environments. WiPE, specifically designed for the extraction of water pixels, generally shows better performance over turbid waters than the standard algorithm developed for Landsat imagery (Fmask). This is explained by the fact that Fmask does not specifically focus on the detection of water pixels, but on the masking of cloud, cloud shadow, and snow over land and water.

Key word: Medium Spatial Resolution Sensors, coastal and inland waters, water pixel extraction, cloud mask.

1. Introduction

Landsat-8, launched on February 11st 2013, carries the Operational Land Imager (OLI) and the Thermal InfraRed Sensor (TIRS). L8-OLI (Table 1) has four spectral bands in the visible, four in the near infrared, and one panchromatic band, while TIRS collects signal within two thermal infrared bands. Recent studies have demonstrated the potential of L8-OLI for ocean color related applications where its medium-spatial resolution (30 m) provides new insights for a better understanding of processes occurring in coastal waters (Pahlevan and Schott, 2013; Vanhellemont and Ruddick, 2014). Atmospheric correction algorithms have been developed to retrieve the remote sensing reflectance ($R_{rs}(\lambda)$, where λ is the

wavelength in nm), from the top of atmosphere (TOA) radiometric signal measured by OLI (Franz et al., 2015; Pahlevan et al., 2017).

Table 1. S2-MSI and L8-OLI spectral bands and spatial resolutions

Sentinel-2			Landsat-8		
Band	**Wavelength (nm)**	**Spatial Resolution (m)**	**Band**	**Wavelength (nm)**	**Spatial Resolution (m)**
1	421 - 457	60	1	433 - 453	30
2	439 - 535	10	2	450 - 515	30
3	537 - 582	10	3	525 - 600	30
4	646 - 685	10	4	630 - 680	30
5	694 - 714	20			
6	731 - 749	20			
7	768 - 796	20			
8	767 - 908	10			
8A	848 - 881	20	5	845 - 885	30
9	931 - 958	60			
10	1338 - 1414	60	9	1360 - 1390	30
11	1539 - 1681	20	6	1560 - 1660	30
12	2072 - 2312	20	7	2100 - 2300	30

Due to the increased radiometric sensitivity from 8-bit to 16-bit data in comparison with the previous Landsat sensors series, the assessment of in water parameters, such as the suspended particulate matter concentration (SPM), the Secchi-disk depth, and the colored dissolved organic matter (CDOM), from $R_{rs}(\lambda)$ is now possible, mainly from empirical and regional approaches, with a relatively good accuracy over coastal waters (Vanhellemont and Ruddick, 2014; Concha and Schott, 2016; Kutser et al., 2016; Lymburner et al., 2016; Lee et al., 2016; Urbanski et al., 2016; Slonecker et al., 2016; Li et al., 2017). A challenge, however, still remains to automatically detect water pixels over which these different

atmospheric and bio-optical algorithms can finally be applied. Cloud and cloud shadow should indeed be correctly detected, which is still rather challenging over coastal and inland waters, bodies that are generally turbid. An over-masking procedure results in a loss of water-pixels, while an under-masking procedure results in a wrong assessment of the remote sensing reflectances and their associated in-water components.

Numerous algorithms have been developed to detect and extract surface water from remote sensing technology for about four decades. For example, the Normalized Difference Vegetation Index (NDVI) (Rouse et al., 1973), based on the red and near-infrared bands, has been used to distinguish land cover from clear to slightly turbid water surface (Vermote & Saleous, 2007 ; Jawak et al., 2015). To specifically identify water pixels, the Normalized Difference Water Index (NDWI), based on the difference between reflectance in the green band, which is greatly impacted by water surface, and the one in the NIR band, has been introduced by McFeeters (1996). However, this very widely used index, cannot efficiently suppress the signal from built-up land and water. Combination of this index with a Geographic Information System (McFeeters, 2013), or modification of this index (MNDWI) by substituting the medium infrared band for the near infrared band (Xue, 2006) have therefore been proposed to improve the detection of water surface in environments with complex signal background. The application of all the latter approaches require manually defined threshold values depending on the study area, which may not be adequate for automatically detecting of water surface pixels whatever the considered environment. Because of its relatively good performance, as well as its full automation, the Fmask (Function of mask) algorithm is commonly used for masking cloud, cloud shadow, and snow in Landsat images (Zhu and Woodcock, 2012). This algorithm is based on predefined thresholds of TOA reflectance values at specific bands, cloud probability calculation, brightness temperature (BT) analysis, NDVI, and normalized difference snow index (NDSI), for many different objects (land, water, cloud shadow, snow, and cloud). Despite the recent improvements of Fmask (Zhu et al., 2015), which take advantage of the new cirrus band for Landsat 8, and which use a dynamic threshold instead of a fixed

one for cloud detection over water, some wrong identifications of water pixels, as those presented in the present study, still remain, especially over turbid waters (see section 4). This is explained by the fact that Fmask does not specifically focus on the detection of water pixels, but on the masking of cloud, cloud shadow, and snow over land and water. In contrast to Fmask, the present study specifically aims at detecting water pixels of inland and coastal waters, and does not specifically focus on the individual identification of each considered object. Because of the high contribution of the Rayleigh component to the TOA signal, its contribution should first be removed for a better characterization of the spectral shape of the reflectance over each object (Nordkvist et al., 2009). For these reasons, the present algorithm, referred to as WiPE in the text (for Water Pixel Extraction), uses the Rayleigh- corrected top of atmosphere reflectance spectra ($\rho_{rc}(\lambda)$) as input parameters. WiPE is based on the combination of spectral criteria applied to $\rho_{rc}(\lambda)$ to mainly discriminate water pixels from land, clouds and vegetation pixels, and on the application of a Hue-Saturation-Value or Brightness, HSV, analysis to optimize the detection of thin clouds and cloud shadow pixels over water areas.

The database of L8-OLI and S2-MSI images collected over contrasted coastal and inland water areas, and dedicated to the development and validation of the algorithm, is first presented. The new algorithm is then described for L8-OLI. Finally, WiPE is evaluated from an independent validation database, and the results are compared with those obtained by Fmask. While the present algorithm is fully described for the OLI sensor, the same methodology is applied to MSI on Sentinel-2a (launched on 23 June 2015) which present some slight differences in terms of spectral bands and spatial resolutions (Table 1). The adaptation of WiPE on S2-MSI is discussed at the end of the paper from illustration examples. This adaptation, performed for S2a-MSI, can fully be applied on S2b-MSI, as the spectral bands of S2a-MS1 and S2b-MSI only differ by about less than one nanometer in the visible and NIR spectral domains.

2. Development and validation data sets

115 *2.1 General description of the satellite data sets*

116 Level-1 of Landsat-8 TOA reflectance and Brightness Temperature (BT) have been downloaded
117 from USGS (https://landsat.usgs.gov/) over different geographical locations covering contrasted
118 atmospheric and environmental conditions (Fig. 1). The whole dataset has been split into two different
119 sub-groups. The first group, gathers 196,738 independent pixels (with 164,681 water pixels) extracted
120 from 32 different scenes, is used for algorithm development. The second one is composed by 12 different
121 scenes for independent testing and validation of the algorithm. The mean and standard deviation values
122 of the sun zenith angle for the development and validation data sets are 28.3°±9.2° and 34.4°±10.1°,
123 respectively. The percentage of cloud cover in the images used for the development and validation data
124 sets are 0.92±14.7 % and 24.6±16.6 %, respectively. The cloud cover is much higher for the validation
125 data set to be able to test the algorithms over a variety of cloud types.

126 The top of atmosphere ($\rho_{TOA}(\lambda)$), as well as the Rayleigh-corrected ($\rho_{rc}(\lambda)$) reflectances are
127 provided over each considered object, which are water, cloud, thin cloud, cloud shadow, construction,
128 barren land, and vegetation. BT, one of the input parameters in Fmask, is also provided over each pixel
129 of each validation scene for the inter-comparison exercise. This dataset covers various bio-optical aquatic
130 environments such as river outlets characterized by brown waters characterized by high (Mekong river
131 delta, Amazon estuary, Rio de la Plata estuary, Gulf of Khambhat) to moderate (south of Hudson bay)
132 suspended sediment loads, green coastal waters with a high concentration of phytoplankton (aquaculture
133 areas in Chinese coastal waters, Halong bay, phytoplankton blooms in Vietnam coastal waters, and in
134 the Liguria sea), and blue offshore waters of the Mediterranean Sea. Water pixels for the development
135 data set have only been selected in coastal and offshore waters to limit mixed water/land situations
136 typically found in inland waters. These different locations have been chosen in order to cover a wide
137 range of water types based on our current knowledge of these specific areas, and on a visual examination
138 of Rayleigh corrected images. This broad range of aquatic environments is reflected in the large

variability of the Rayleigh-corrected reflectance spectra, $\rho_{rc}(\lambda)$, extracted over water pixels (Fig. 2). The amplitude and spectral position of the maximum of $\rho_{rc}(\lambda)$, mainly driven by the bio-optical properties of the water body span over a large range of values. For instance, the maximum of $\rho_{rc}(\lambda)$ is observed at band 1, 2, 3, 4, and 5 for 2.3%, 22.9%, 45.4%, 26.6%, and 2.8% of the water pixels used in the development data set (Fig. 2), respectively. This spectral shift reflects a change in the turbidity level, as the maximum of water remote sensing reflectance is observed in the blue and near-infrared for clear and very turbid waters, respectively (Han et al., 2016).

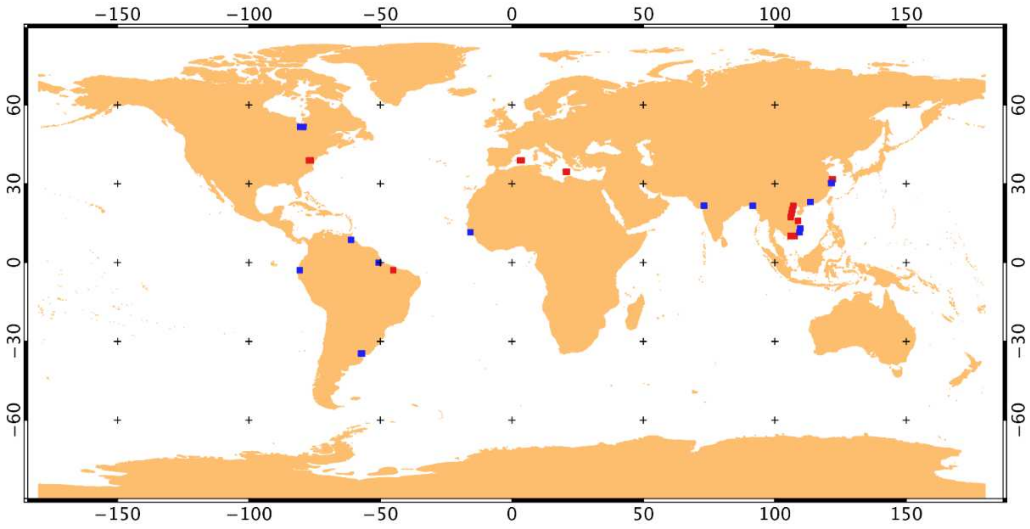

Fig. 1. Location of L8-OLI images used for the development (red dots, 32 different scenes) and validation (blue dots, 12 different scenes) steps of the algorithm.

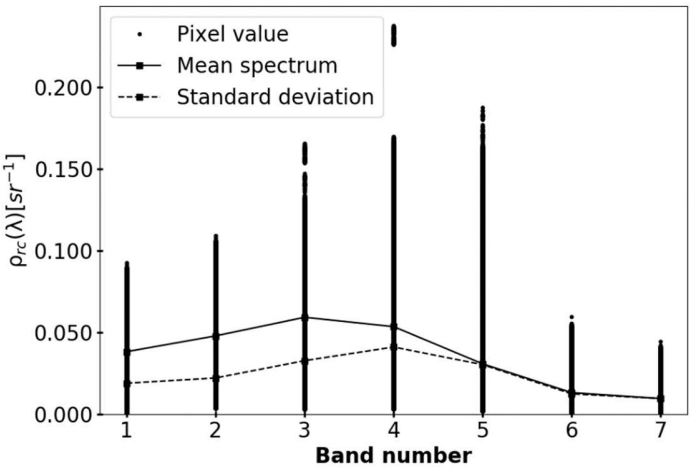

151

152 **Fig. 2.** Mean and standard deviation of $\rho_{rc}(\lambda)$ spectra over the 164,681 selected water pixels of the
153 developing data set for L8-OLI.

154

155 In contrast to L8-OLI where each visible and NIR spectral channels used in WiPE have the same
156 spatial resolution (i.e. 30 m), the MSI-S2 relevant channels present some discrepancies in terms of spatial
157 resolution (Table 1). Following the two steps approach developed for L8-OLI, WiPE is adapted to S2-
158 MSI based on a development data set of 65 S2-MSI images collected from
159 https://scihub.copernicus.eu/dhus in contrasted aquatic environments (European, South America,
160 Vietnam, and China coastal waters). Considering the similar performance of WiPE on S2-MSI and L8-
161 OLI images (not shown here), and because the validation of WiPE is deeply examined for OLI in the
162 present paper, we will only discuss the performance of WiPE for S2-MSI observations on two
163 representative examples, the Huangmao river estuary (China) and the Tonle Sap lake (Cambodia). We
164 will specifically focus on the impact of the MSI per-channel spatial resolution variation.

165

166 *2.2. The Rayleigh correction procedure*

In order to better characterize the spectral signature of the different selected objects, the signal due to air molecules, which contributes to a large part of $\rho_{TOA}(\lambda)$, should be removed. The TOA reflectance, $\rho_{TOA}(\lambda)$, can be developed as follows (Gordon, 1997):

$$\rho_{TOA}(\lambda) = \rho_R(\lambda) + \rho_a(\lambda) + \rho_{Ra}(\lambda) + T(\lambda)\rho_g(\lambda) + t(\lambda)\rho_{wc}(\lambda) + t(\lambda)\rho_w(\lambda) \quad (1)$$

where $\rho_R(\lambda)$ is the reflectance due to multiple scattering of a purely air molecules atmosphere, $\rho_a(\lambda)$ is the reflectance of multiple scattering by aerosols in a pure aerosol atmosphere, and $\rho_{Ra}(\lambda)$ stands for the interaction term in a real atmosphere containing both molecules and aerosols. $T(\lambda)$ and $t(\lambda)$ are the direct and diffuse transmittances of the atmosphere, respectively. $\rho_g(\lambda)$, $\rho_{wc}(\lambda)$, and $\rho_w(\lambda)$ are the reflectances due to sun glint, whitecaps, and in-water optically significant components, respectively. The sunglint and whitecaps reflectances are related to wind speed and geometry (Wang and Bailey, 2001).

The pixel value recorded by L8-OLI at the top of the atmosphere is a digital number, from which the TOA radiance, $L_{TOA}(\lambda)$, and reflectance, $\rho_{TOA}(\lambda)$, are calculated through Eq.(2) and Eq.(3), respectively (Vanhellemont and Ruddick, 2014).

$$L_{TOA}(\lambda) = M_L(\lambda)Q_{cal}(\lambda) + A_L(\lambda) \quad (2)$$

$$\rho_{TOA}(\lambda) = \frac{\pi L_{TOA}(\lambda)d^2}{F0(\lambda)cos(\theta_0)} \quad (3)$$

where $L_{TOA}(\lambda)$ is the spectral radiance (in W m^{-2} sr^{-1} μm^{-1}), $M_L(\lambda)$ the radiance multiplicative scaling factor (i.e. gain) for each band, $Q_{cal}(\lambda)$ the Level-1 pixel value in digital number, and $A_L(\lambda)$ is the radiance additive scaling factor (i. e. offset) for each band. d, F0, and θ_0 are the Earth-Sun distance in Astronomical Units, the band average solar irradiance, and the sun zenith angle, respectively.

The reflectance due to Rayleigh scattering in a purely molecular atmosphere, $\rho_R(\lambda)$, is given by the following equation (Gordon et al., 1988; Wang and King, 1997):

$$\rho_R(\lambda) = \tau_R(\lambda) p_R(\Theta)(4cos\theta_0 cos\theta_v)^{-1} \quad (4)$$

where $\tau_R(\lambda)$ is the Rayleigh scattering optical thickness, $p_R(\Theta)$ the Rayleigh scattering phase function at a scattering angle, Θ, θ_v the viewing zenith angle, and θ_0 the sun viewing angle. The optical thickness at the atmospheric pressure P is calculated as follows:

$$\tau_R(\lambda) = \frac{P}{P_0}\tau_{R0}(\lambda) \quad (5)$$

where $\tau_{R0}(\lambda)$ is the optical thickness at the standard atmospheric pressure P_0 of 1013.25 mbar.

The Rayleigh scattering phase function $p_R(\Theta)$ is defined as:

$$p_R(\Theta) = P_R(\Theta_-) + [r(\theta_v) + r(\theta_0)]P_R(\Theta_+) \quad (6)$$

The term involving Θ_- provides the contribution due to photons which are backscattered from the atmosphere without interacting with the sea surface. The term involving Θ_+ accounts for photons which are scattered in the atmosphere toward to the sea surface. These terms are computed from sun-sensor geometry as:

$$cos(\Theta_\pm) = \pm cos(\theta_0)cos(\theta_v) - sin(\theta_0)sin(\theta_v)cos|\phi_0 - \phi_v| \quad (7)$$

with $\phi_0$and $\phi_v$are sun and sensor azimuth angles. $r(\theta)$ is the Fresnel reflectance for air-incident rays at incidence angle θ. The Rayleigh scattering phase function $P_R(\Theta)$for scattering angle Θ, and the Fresnel reflectance $r(\theta)$ for air-incident rays at an incidence angle θ are calculated as follows:

$$P_R(\Theta) = \frac{3}{4}\left(1 + cos^2(\Theta)\right) \quad (8)$$

$$r(\theta) = 0.5\left\{\frac{sin^2(\theta-\theta_t)}{sin^2(\theta+\theta_t)} + \frac{tan^2(\theta-\theta_t)}{tan^2(\theta+\theta_t)}\right\} \quad (9)$$

$$\theta_t = sin^{-1}\left(n_w sin(\theta)\right) \quad (10)$$

The Rayleigh-corrected reflectance is defined in Eq.(11) as:

$$\rho_{rc}(\lambda) = \rho_{TOA}(\lambda) - \rho_R(\lambda) = \rho_a(\lambda) + \rho_{Ra}(\lambda) + T(\lambda)\rho_g(\lambda) + t(\lambda)\rho_{wc}(\lambda) + t(\lambda)\rho_w(\lambda) \quad (11)$$

Rayleigh scattering generally contributes about 80% to 90% of the TOA reflectance in the blue part of the spectrum from clear to turbid waters, respectively (Gordon et al., 1988; IOCCG, 2010).

2. 3. Spectral database for each selected object

Classified objects are manually selected on Rayleigh-corrected color image composites. Polygons are drawn over homogenous areas of the considered objects, and pixels are counted using the QGIS software. Mixed situations are manually disregarded, except those specifically considered here as cloud shadows and thin clouds over land and water. All TOA reflectance and Rayleigh-corrected spectra are stored for each of the following objects: clouds over land and water (664 pixels), thin clouds over land and water (9493 pixels), shadows over land and water (13,582 pixels), water (164,681 pixels), vegetation (4817 pixels), barren land (2103 pixels), and constructions (1398 pixels). The whole database of the $\rho_{rc}(\lambda)$ spectra over the six non-water selected objects is provided in Fig. 3. Similarly to the water pixels (Fig. 2), each of the previous object is characterized by a large range of variability of $\rho_{rc}(\lambda)$ spectra, as shown by the large standard deviations observed around each mean spectrum. Based on this latter pattern, we can assume that the database covers a broad range of situations for each object, which makes it quite suitable for the algorithm development phase.

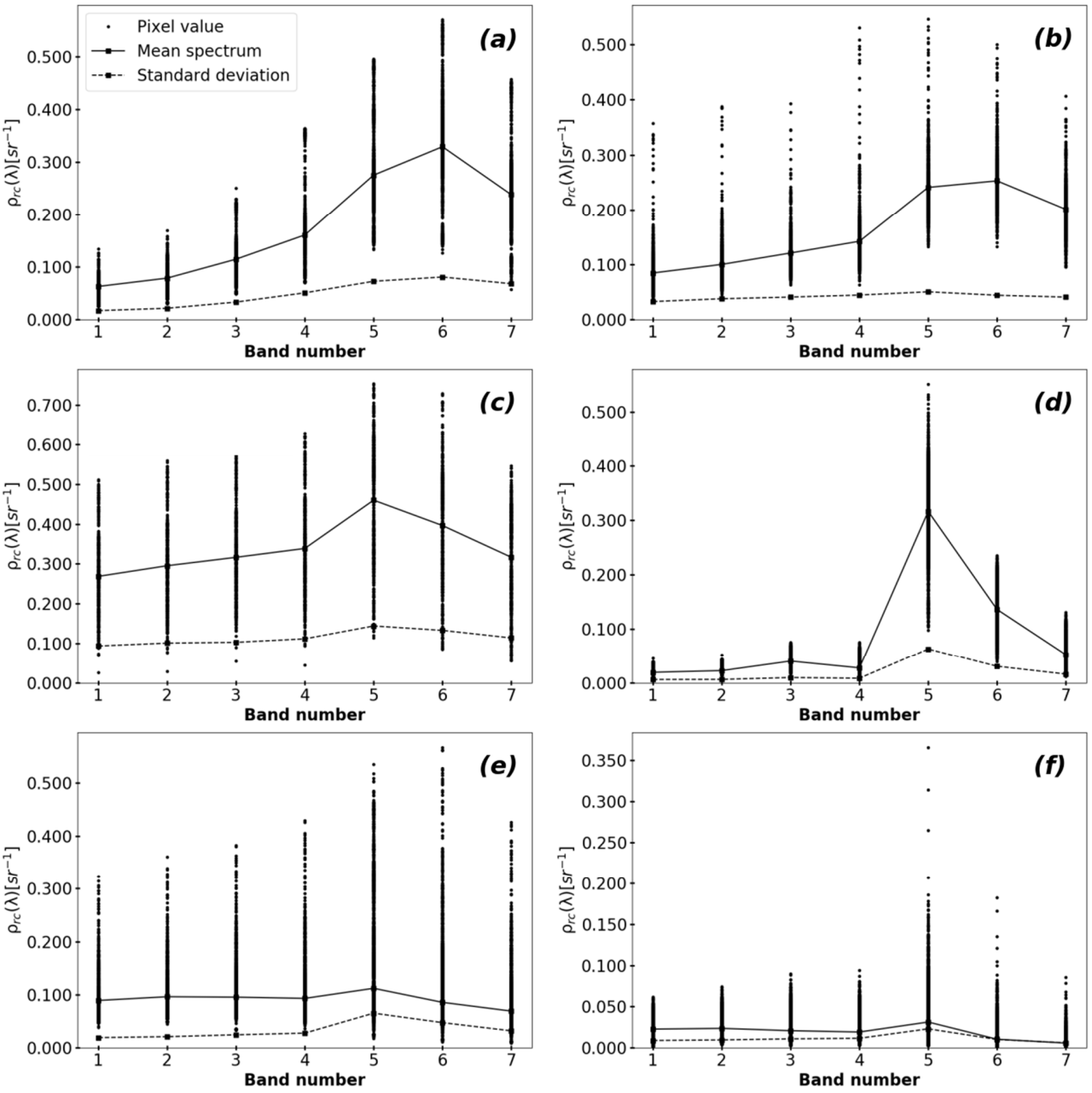

225

226 **Fig. 3.** Mean and standard deviation of $\rho_{rc}(\lambda)$ spectra collected by L8-OLI over (a) barren land, (b)
227 construction, (c) clouds over land and water, (d) vegetation, (e) thin clouds over land and water, and (f)
228 cloud shadows over land and water.

229

The benefit of using $\rho_{rc}(\lambda)$ instead of $\rho_{TOA}(\lambda)$ to detect water pixels is illustrated in Fig. 4, where typical spectra over water bodies are displayed. From clear (Fig. 4a) to very turbid waters (Fig. 4d) the spectral shape (as well as the amplitude) of $\rho_{rc}(\lambda)$ significantly differs from one water type to another. These latter spectral shape differences are less pronounced for $\rho_{TOA}(\lambda)$, especially between clear (Fig. 4a) and green water (Fig. 4b).

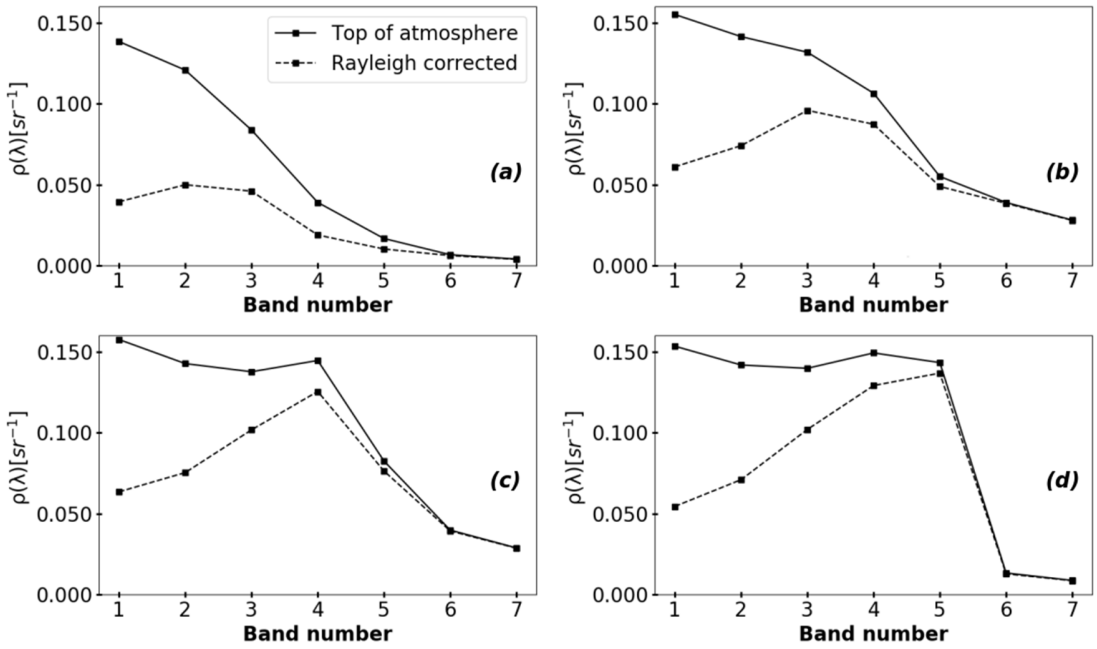

Fig. 4. Different $\rho_{rc}(\lambda)$ and $\rho_{TOA}(\lambda)$ spectra collected by L8-OLI over (a) blue (i.e. clear) (b) green, (c) turbid, and (d) very turbid water areas.

3. Development of the new algorithm (referred to as WiPE)

3. 1. General approach

While the average $\rho_{rc}(\lambda)$ spectra for the different identified objects present significant differences in terms of spectral shape and amplitude, the associated large standard deviation values (Fig. 3) also stress a potential overlap between them. This patterns has oriented the development of the algorithm

244 through the use of a clustering approach developed in different spaces generated by the combination of
245 $\rho_{rc}(\lambda)$ (or $\rho_{rc}(\lambda)$ ratios) spectral values (first step of the algorithm), or by the combination of $\rho_{rc}(\lambda)$, V,
246 and S values of the HSV transformation (second step of the algorithm).

247 Typical examples of $\rho_{rc}(\lambda)$ spectra, which allow the understanding of the different spectral criteria
248 adopted in WiPE, are displayed over the six non-water objects in Fig. 5. With a relatively sharp increase
249 of $\rho_{rc}(\lambda)$ from band 1 (blue) to band 5 (near infrared), the barren land (Fig. 5a) and construction spectra
250 (Fig. 5b) significantly differ from other objects. This spectral shape, combined with the high peaks in
251 bands 5 (near infrared) and 6 (short wave infrared), allow barren land (Fig. 5a), and construction (Fig.
252 5b) to be distinguished from the other objects. In the same way, the sharp increase of $\rho_{rc}(\lambda)$ observed
253 between bands 4 and 5 for vegetation pixels (Fig. 5d) is a remarkable identification pattern of the
254 corresponding pixels. Further, the relatively flat $\rho_{rc}(\lambda)$ spectral shape, associated with a high level of
255 signal in the blue-red part of the spectrum, allow clouds to be relatively well identified from other objects
256 (Fig. 5c). Based on these observations, criteria have been developed on the spectral shape and amplitude
257 of $\rho_{rc}(\lambda)$ spectra in order to distinguish water pixels from land (vegetation, barren land, and construction)
258 and clouds over water. The application of these different spectral criteria represents the first step of the
259 algorithm (Fig. 6). In contrast to the previous objects, the $\rho_{rc}(\lambda)$ spectra over thin cloud (Fig. 5e) and
260 shadow (Fig. 5f) pixels may strongly be modified by the spectra of the overlaid water pixels which makes
261 the identification of these two objects over water areas very challenging from spectral shape analysis as
262 performed in the first step of the algorithm. For that purpose, the second step of the algorithm is based
263 on a multispectral colorimetric method, i. e., HSV transformation, which allows a better identification of
264 water pixels in these difficult configurations (Fig. 6).
265

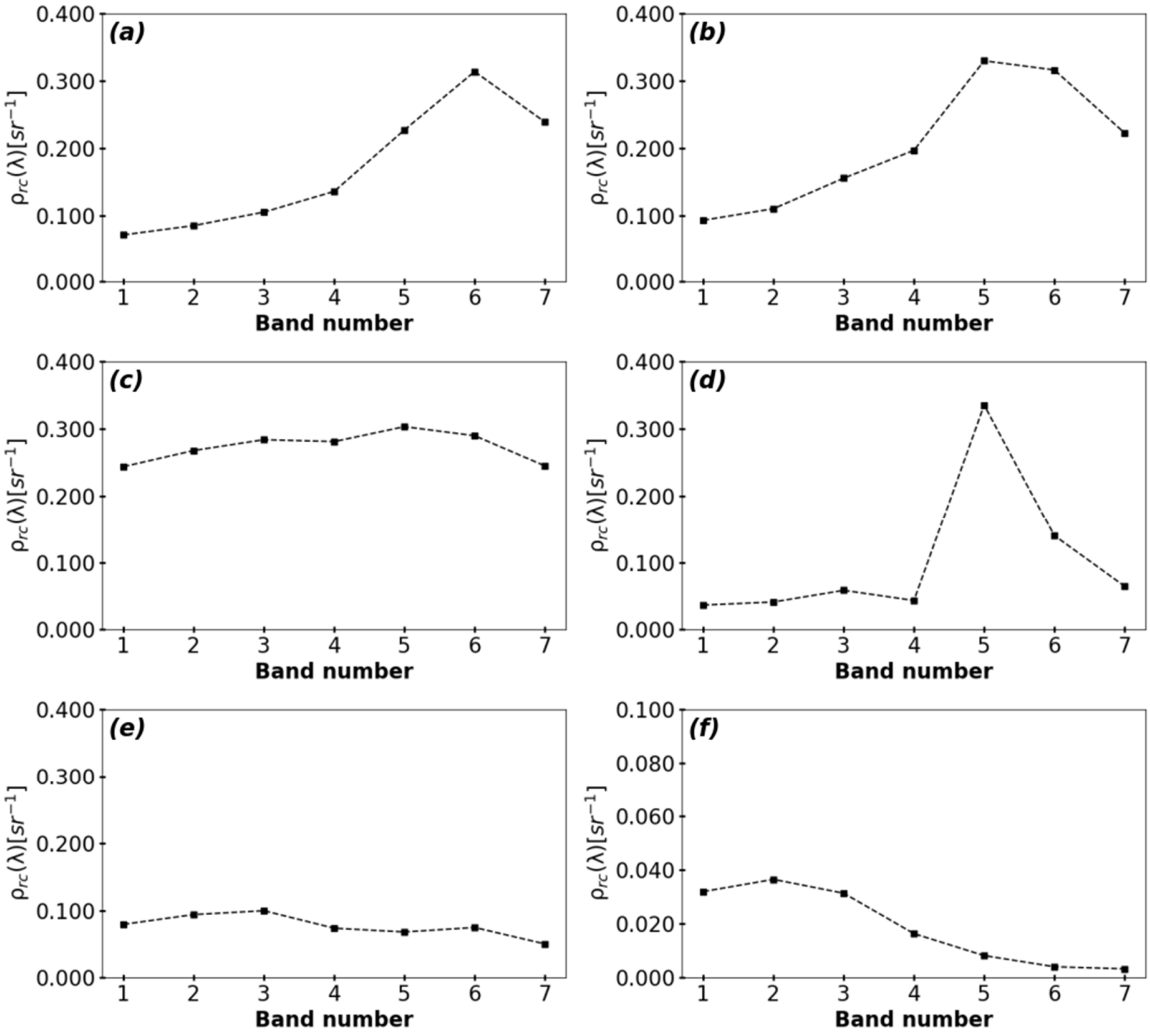

Fig. 5. Examples of $\rho_{rc}(\lambda)$ spectra collected by L8-OLI over the following non-water objects:(a) barren land, (b) construction, (c) clouds over water, (d) vegetation, (e) thin clouds over green water, and (f) clouds shadow over clear water.

3.2. First step of the algorithm: the spectral shape analysis

Spectral shapes and amplitude of $\rho_{rc}(\lambda)$ spectra over all objects are used for the algorithm development. Some objects with specific $\rho_{rc}(\lambda)$ spectral signature will be masked in the first step (Fig. 6). This is the case of vegetation, barren land, construction, clouds, and shadow over land that will be removed based on some different combinations of $\rho_{rc}(\lambda)$ band ratios. Standard indexes, as those presented

in the introduction (e.g. NDWI; MNDWI), have also been tested but they did not provide any better results compared to those selected for step 1. The different equations and threshold values used in the two steps of the WiPE algorithm and presented in the flowchart (Fig. 6), have been empirically defined from visual examination of the data points in the different considered (x; y) spaces (Fig. 7).

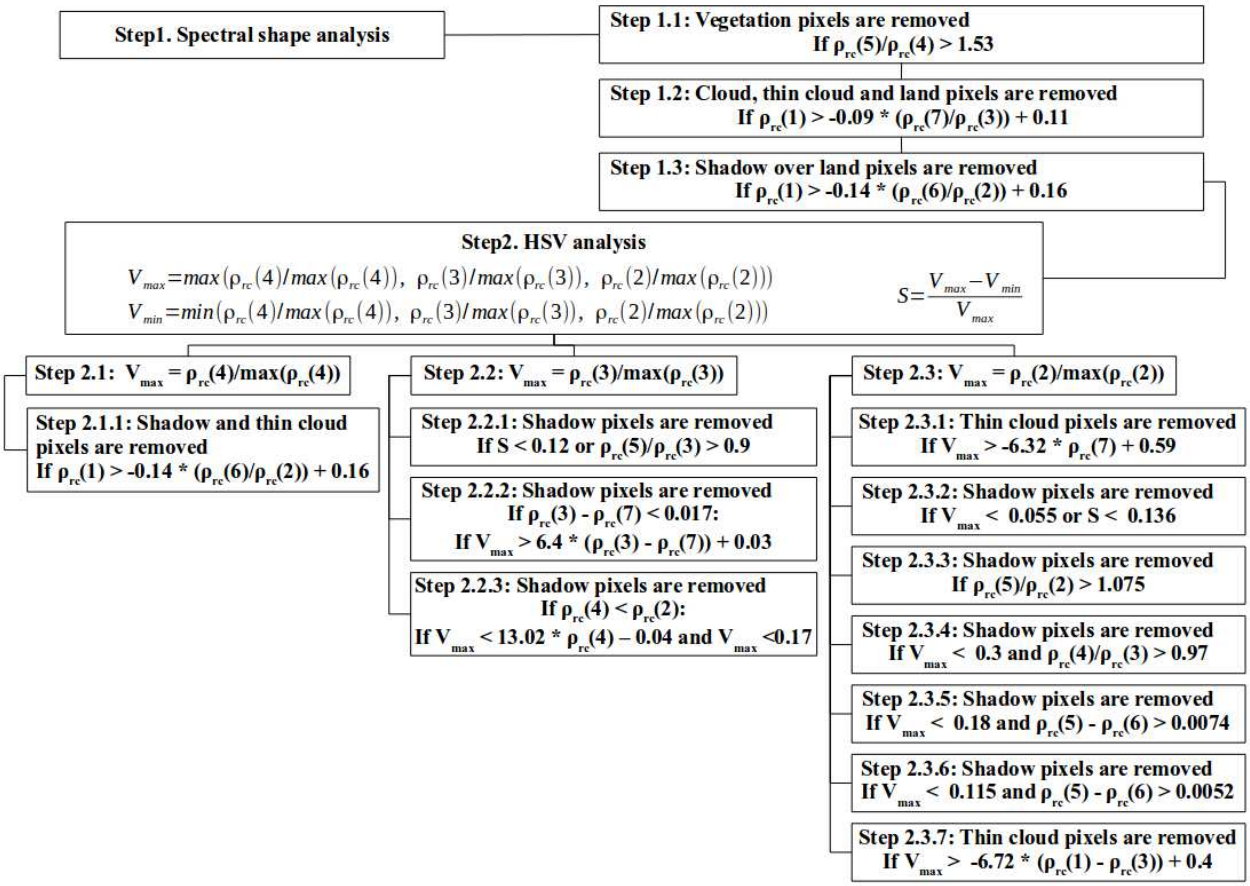

Fig. 6. The logic flow of the water extraction pixel algorithm based on the combination of spectral shape analysis (step 1) and HSV analysis (step 2) for the L8-OLI sensor. This flowchart requires the Rayleigh corrected reflectance (Eq.11) at bands 1, 2, 3, 4, 5, 6, and 7 as input parameters.

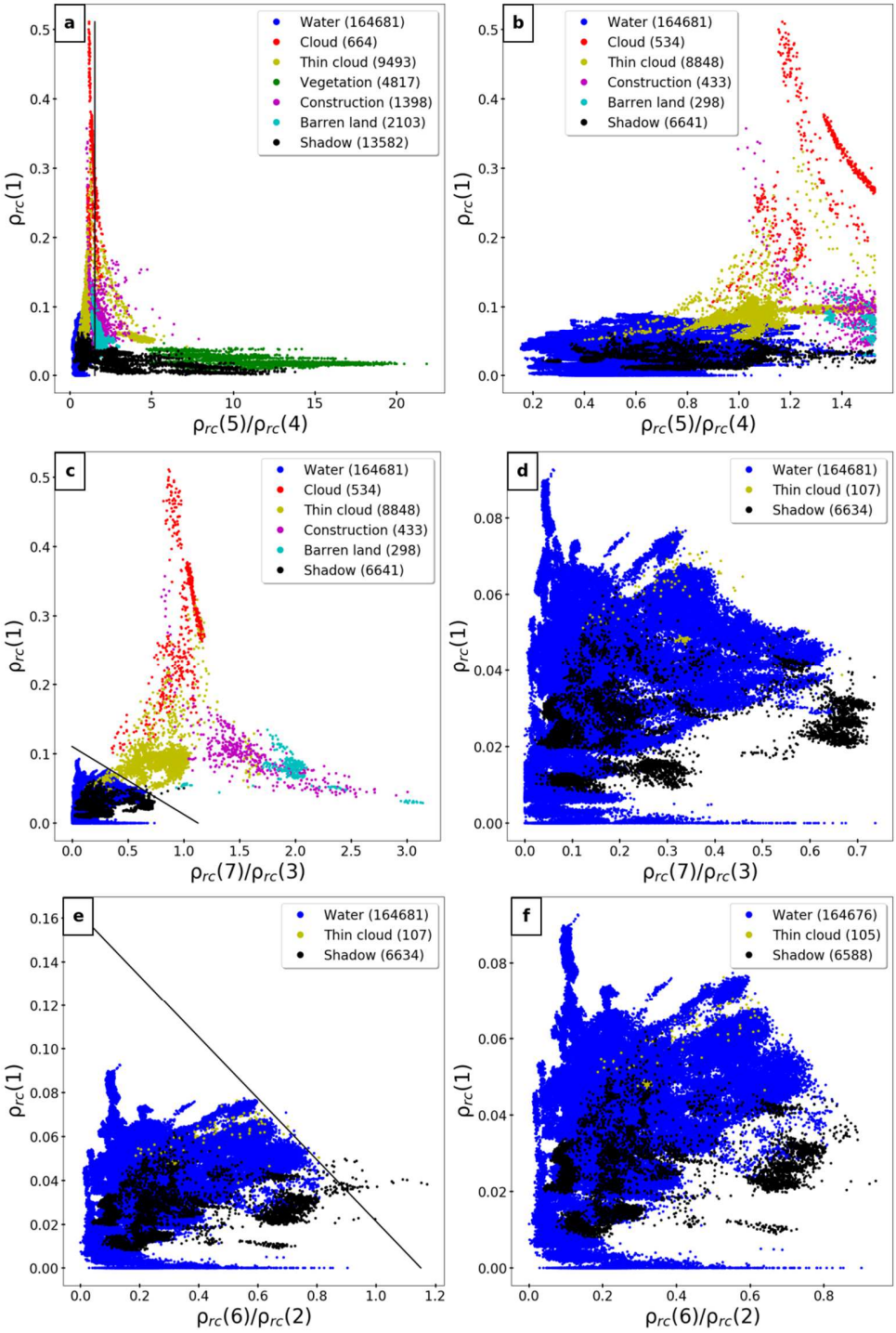

283

284 **Fig. 7.** (left panels) Scatter plots of $\rho_{rc}(\lambda)$ as a function of $\rho_{rc}(\lambda)$ band ratios for the seven different objects
285 of the development data set. The black line corresponds to the limit adopted to remove (a) vegetation
286 (step 1.1), (c) clouds, construction, and barren land (step 1.2), and (e) cloud shadow over land pixels
287 (step 1.3). Each color corresponds to a different object as indicated. The number of pixels before (panels

288 a, c, and e) and after (panels b, d, and f) the application of each criterion adopted in steps 1.1, 1.2, and
289 1.3 are provided in each panel.
290
291 Because of their very specific spectral signatures in the NIR domain (Figure 5d), vegetation pixels
292 are the first to be removed (step 1.1 in Fig. 6). Pixels with near infrared to red ratio value, $\rho_{rc}(5)/\rho_{rc}(4)$,
293 greater than 1.53 are identified as vegetation in the ($\rho_{rc}(5)/\rho_{rc}(4)$; $\rho_{rc}(1)$) space (Fig. 7a). This threshold
294 value, manually fixed based on the examination of the data points in the ($\rho_{rc}(5)/\rho_{rc}(4)$; $\rho_{rc}(1)$) space,
295 allows vegetation pixels to be remarkably well separated from water pixels (Fig. 7b), avoiding the mixing
296 of water and vegetation pixels even over very challenging situations such as inland productive waters. In
297 addition to removing the totality of the vegetation pixels, the application of this ratio also removed many
298 pixels from other objects, such as barren land (86%), thin clouds (7%) and almost all shadow pixels over
299 land (Fig. 7b). Clouds over land and water pixels present the highest Rayleigh-corrected reflectance in
300 almost every bands (Fig. 5c), but because of the high range of variability observed at each band, cloud
301 pixels may be difficult to distinguish from barren land (Fig. 5a) and construction (Fig. 5b) pixels which
302 present relatively similar spectral shape. For this reason, cloud over water and land, barren land, and
303 construction pixels are removed simultaneously at the step 1.2, using a combination of $\rho_{rc}(1)$ and
304 $\rho_{rc}(7)/\rho_{rc}(3)$ (see step 1.2 in Fig. 6). When $\rho_{rc}(1)$ is higher than $-0.09*\rho_{rc}(7)/\rho_{rc}(3) + 0.11$ the pixel is
305 rejected (Fig. 7c). By pulling cloud, barren land, and construction all together, this test will not allow for
306 a specific identification of these three different objects. However, that specific identification of non-water
307 objects is not the objective of the present method, which is only dedicated to the extraction of free water
308 pixels. Interestingly, this test also removed almost all thin clouds (Fig. 7d) over land and waters (98.9%).
309 The remaining thin-cloud pixels (1.1%) after the application of this first step are only found over water
310 pixels (Fig. 7d).

311 Shadow pixels are by essence difficult to remove, due to their relatively low reflectance value
312 and the strong impact of the spectral shape of the overlaid object. Based on the development database,
313 identified shadow pixels over land present a minimum $\rho_{rc}(2)$ value, while almost all land objects have
314 $\rho_{rc}(6) > \rho_{rc}(2)$. For that purpose the $\rho_{rc}(6)/\rho_{rc}(2)$ ratio, which presents a large range of variability, is
315 plotted against $\rho_{rc}(1)$, for which shadow pixels over land show the lowest variability compared to other
316 bands (Fig. 5f). Based on these observations, pixels with $\rho_{rc}(1)$ higher than $-0.14*\rho_{rc}(6)/\rho_{rc}(2) + 0.16$ are
317 rejected (Fig.7e). The application of this criterion allows one to remove the remaining shadow pixels
318 over land that were still present after step 1.1. Only shadow pixels over water remain (the black dots in
319 Fig. 7f). Shadow pixels over water or land can be distinguished from one another, because, while the
320 $\rho_{rc}(\lambda)$ signal over these two different objects is undoubtedly attenuated by clouds shadow, the marked
321 differences in their spectral shapes are still noticeable, allowing the differentiation between shadow over
322 land and shadow over water. The performance of the spectral shape analysis procedure is illustrated over
323 a very complex aquaculture area at Rio Guayas in Ecuador where water and vegetation areas are
324 especially difficult to distinguish from one another on the Red-Green-Blue (RGB) composite (Fig. 8a).
325 Distinction between waters and vegetation/land/clouds pixels is very well performed. This has been
326 confirmed by a visual examination of images provided on google earth allowing a distinct identification
327 of aquaculture farms. However, while cloud shadows over land are appropriately masked, cloud shadows
328 areas over water (red circles in Fig. 8a) are misleadingly identified as water.
329

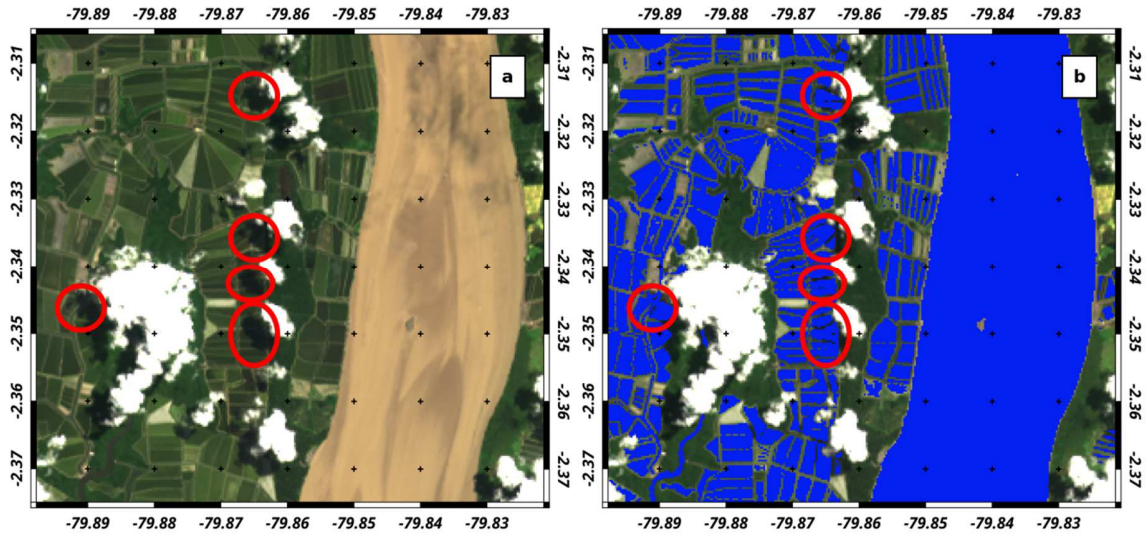

Fig. 8. (a) RGB image collected by L8-OLI over an aquaculture area at Rio Guayas in Ecuador (17/05/2015). (b) water pixel extraction (in blue) showing the performance of the spectral shape analysis (first step) to distinguish vegetation/cloud/land and water pixels in such challenging environment. At this stage (step 1), pixels with shadow over water are still not removed and are falsely identified as water (see red circles).

3.3. Second step of the algorithm: the HSV approach

Based on the spectral shape analysis developed in the first step of the algorithm, cloud over land and water, shadow over land, vegetation, barren land, and construction pixels are remarkably well removed. At this stage, only water pixels, thin clouds and shadow over water pixels remain. Cloud shadow pixels over water may therefore falsely be considered as water (Fig. 8). The significant differences observed in the $\rho_{rc}(\lambda)$ spectral shape over turbid (Fig. 9a), green (Fig. 9c), and clear (Fig. 9e) waters fade away in presence of shadow (Fig. 9b, d, and f). For this reason, Rayleigh-corrected reflectance spectra are transferred into the HSV color space which uses Hue, Saturation, and Value for color representation. In contrast to the standard RGB color space, where the color information and its intensity are generally mixed, the HSV color space is better adapted for image analysis and segmentation

(Smith, 1978; Ganesan et al., 2014). For instance, this color transformation, based on a mechanism of human model, has facilitated the extraction of water pixels over land (Pekel et al., 2014; Singh et al., 2016), and the correction of thin clouds which have high brightness, low saturation, and contrast (Pratt et al., 2001; Shen et al., 2015).

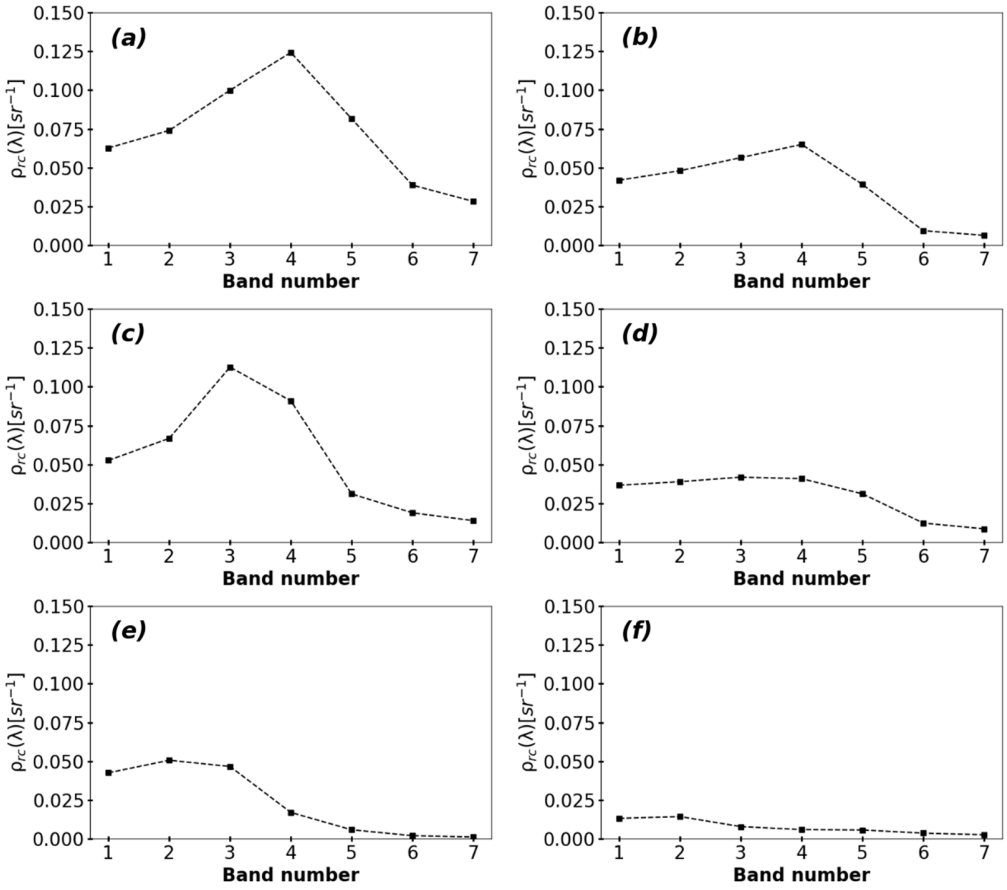

Fig. 9. Left panels - $\rho_{rc}(\lambda)$ spectra collected by L8-OLI over (a) turbid water, (c) green water, and (e) blue water. Right panels - $\rho_{rc}(\lambda)$ spectra for shadow pixels over (b) turbid water, (d) green water, and (f) blue water.

Hue is the angular component and indicates the color relative to the wavelength. The Hue component values, H, range between 0° to 360°, and represents the Hue of red (from 0° to 60°), yellow

359 (from 60° 120°), green (120° to 180°), etc. The Saturation component, S, is determined by the
360 combination of light intensity and how much it is distributed across the spectrum. It describes how white
361 the color is (a white object has a S value of 0). For instance, a pure green is fully saturated, with a
362 saturation of 1 while tints of green have saturations less than 1. At last, the Value component, V, describes
363 the intensity (or brightness) of the color of a considered pixel for a given image. In contrast to H, both S
364 and V values are between 0 and 1. Because the Hue of the ground object is relatively invariant in presence
365 of thin clouds (Shen et al., 2015), only the value, V, and saturation, S, will be taken into account in the
366 present algorithm. The S and V values of the Rayleigh-corrected spectra are calculated as follows:

367 $$S = \frac{(V_{max} - V_{min})}{V_{max}} \quad (12)$$

368 with V_{max} and V_{min} defined as:

369 $$V_{max} = max\left(\frac{\rho_{rc}(4)}{max(\rho_{rc}(4))}, \frac{\rho_{rc}(3)}{max(\rho_{rc}(3))}, \frac{\rho_{rc}(2)}{max(\rho_{rc}(2))}\right) \quad (13)$$

370 $$V_{min} = min\left(\frac{\rho_{rc}(4)}{max(\rho_{rc}(4))}, \frac{\rho_{rc}(3)}{max(\rho_{rc}(3))}, \frac{\rho_{rc}(2)}{max(\rho_{rc}(2))}\right) \quad (14)$$

371 where $\max \rho_{rc}(i)$ represents the maximum value of $\rho_{rc}(i)$ observed over the whole image for
372 the band i. Depending on the spectral band where V_{max} is obtained, different criteria involving V_{max} and
373 S are applied to extract shadow as well as thin cloud pixels over water (Fig. 6). Importantly, in contrast
374 with the first step which is a pixel per pixel approach, the maximum values are here assessed over the
375 whole scene. Figure 10 shows the remaining pixels identified in Figure 7f and transferred into HSV space
376 for the three possible values of V_{max}: when V_{max} is observed in the red (Fig. 10a,b), green (Fig. 10c, d),
377 and blue (Fig. 10e, f). The sum of the water, thin clouds, and shadow pixels observed in Fig 10a, c, and
378 e is equal to the number of water, thin clouds, and shadow pixels at the end of step 1 (Fig. 7f). When
379 V_{max} is reached at band 4 (red) (Fig. 10 a, b), shadow pixels and thin clouds are removed if $\rho_{rc}(1)$ is
380 higher than $-0.14*\rho_{rc}(6)/\rho_{rc}(2) + 0.16$. This condition allows 69% of the shadow pixels over turbid waters,
381 and 50% of the few remaining thin clouds to be removed. The remaining shadow pixels are observed in

382 a restricted area of the $V(\rho_{rc}(4))$ vs. $\rho_{rc}(4)/\rho_{rc}(2)$ space (Fig. 10b) where there is a risk of confusion. A
383 flag, indicating the potential presence of cloud shadows over water pixels, can be raised when the pixel
384 belongs to this restricted space. When V_{max} is reached at band 3 (green) (Fig. 10 c, d) or 2 (blue) (Fig. 10
385 e, f), shadow pixels and thin clouds are removed after the application of three or seven complementary
386 criteria as defined in Fig. 6, respectively. In contrast to turbid waters, where the maximum of ρ_{rc} is
387 generally observed in the red, extraction of shadow pixels over green and blue waters is more challenging.
388 For instance, only 40% and 30% of shadow pixels over green and blue waters have been removed by the
389 HSV approach, respectively. However, these relatively clear water pixels are located in relatively
390 offshore waters, especially the blue ones, for which the signal over noise ratio of OLI prevents the
391 exploitation of this signal for bio-optical applications. The full processing (i. e. step 1 + step 2) of the
392 image collected over a complex aquaculture area discussed previously (Fig. 8), and not used in the
393 development data set, is now provided in Fig. 11. Cloud shadow pixels, falsely identified as water pixels
394 after the application of the spectral shape analysis (Fig. 11a), are now well classified at the second step
395 of the algorithm (Fig. 11b).
396

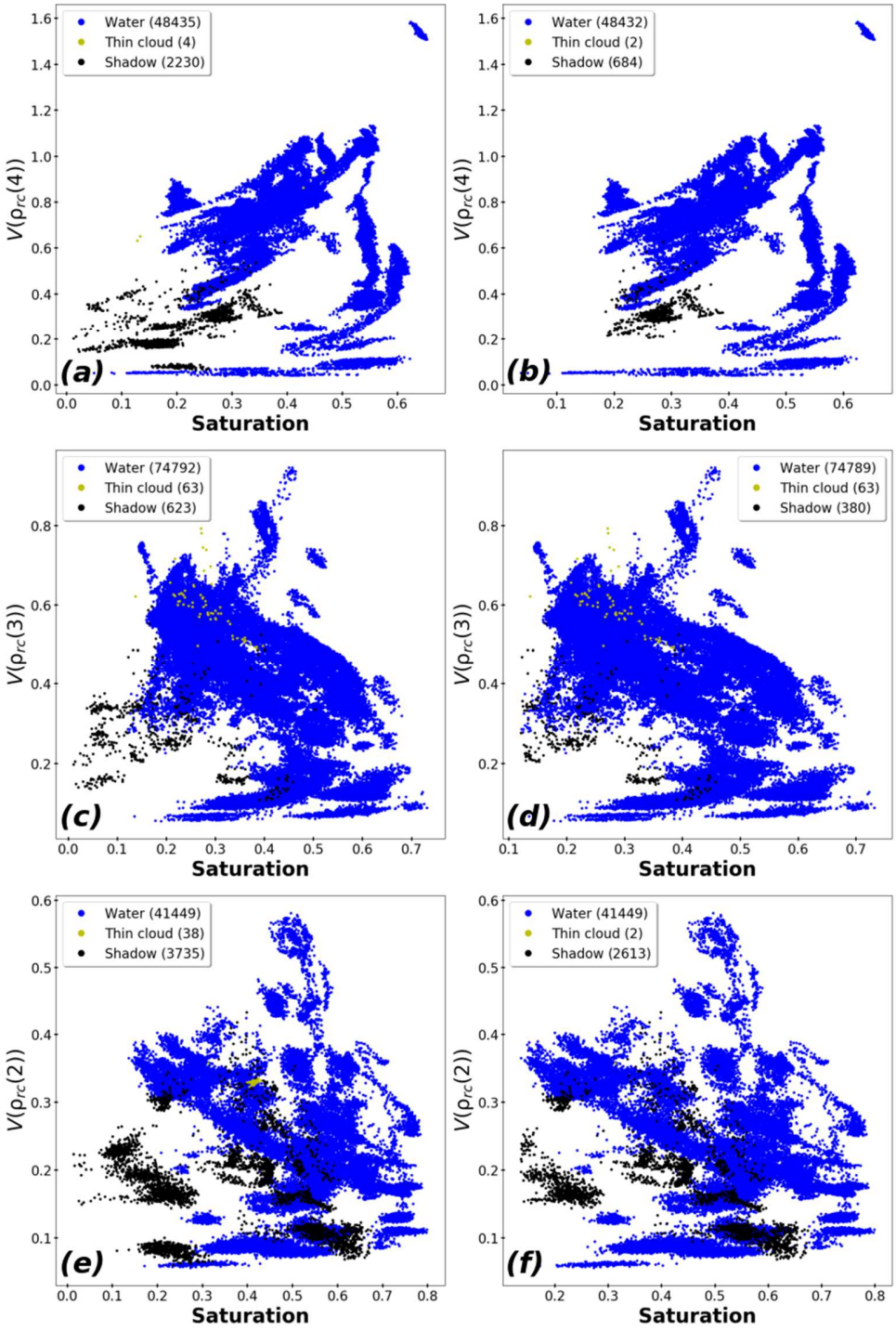

Fig. 10. Scatter plots of the Value component as a function of the Saturation component in the red (panels a and b), green (panels c and d), and blue (panels e and f) for the water (blue dots) and shadow pixels above water (black dots). The number of pixels before (panels a, c, and e) and after (panels b, d, and f) the application of each criterion adopted in steps 2.1, 2.2, and 2.3 are provided in each panel.

402

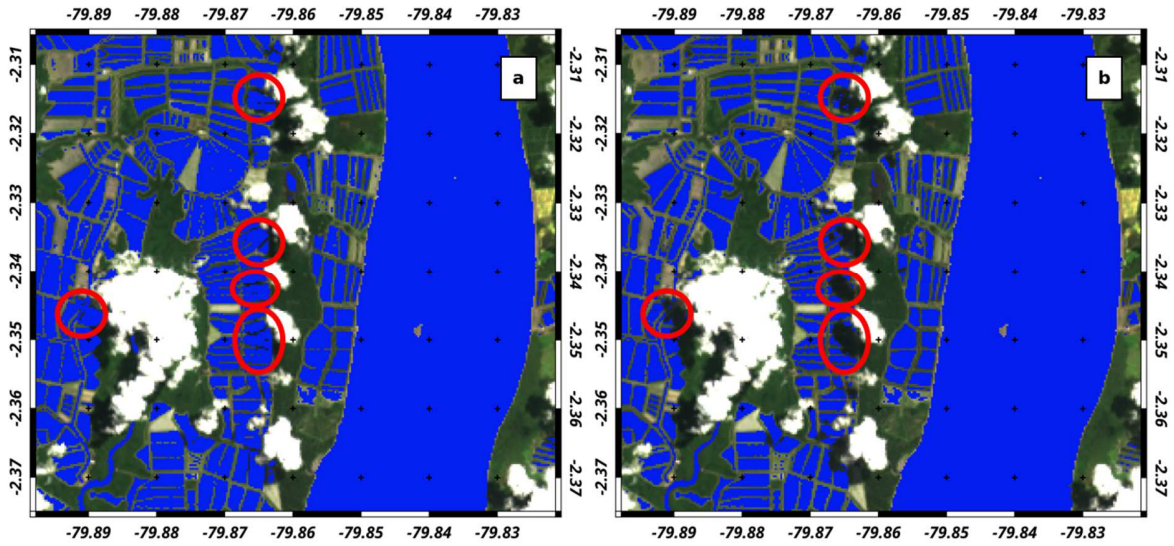

403

404 **Fig. 11.** (a) Water pixel extraction (in blue) after the application of the first step of the algorithm over
405 the aquaculture area at Rio Guayas presented in Fig. 8. (b) as (a) but after the application of the second
406 step of the algorithm showing the identification of the cloud shadow pixels over water. See Fig. 8 for the
407 RGB image.

408

409 **4. Application of WiPE to OLI and comparison with Fmask over contrasted water bodies**

410

411 The WiPE algorithm is based on the use of spectral relationships empirically established on a
412 given development data set, and cannot, by essence, account adequately for all situations encountered,
413 especially for mixed situations (i. e. flooded land, clouds and clouds shadow boundaries, bottom albedo
414 in very clear shallow waters, mountain areas, etc). For example, the spectral shape of $\rho_{rc}(\lambda)$ over water
415 pixels can also be affected by the bottom albedo in very clear shallow waters, especially in the blue and
416 green parts of the spectrum. While the differentiation between cloud (or land) and water pixels should
417 not be affected by the bottom albedo due to the relatively low water reflectance compared to the cloud

418 (or land) reflectances, this may represent an issue for masking shadow and thin clouds pixels over water.
419 This issue can only be addressed by adding a flag cautioning for potential confusion in the processing
420 scheme for clear and very shallow aquatic environment. Adjacency effects may also be another source
421 of uncertainty in the border areas between different objects. The detection of water pixels in mountain
422 areas is also very challenging, due to numerous shadow areas and adjacency effects. The application of
423 WiPE to a complex mountain area in the North West of China shows however that water pixels are still
424 well identified in such complex environment (Fig. 12).
425
426

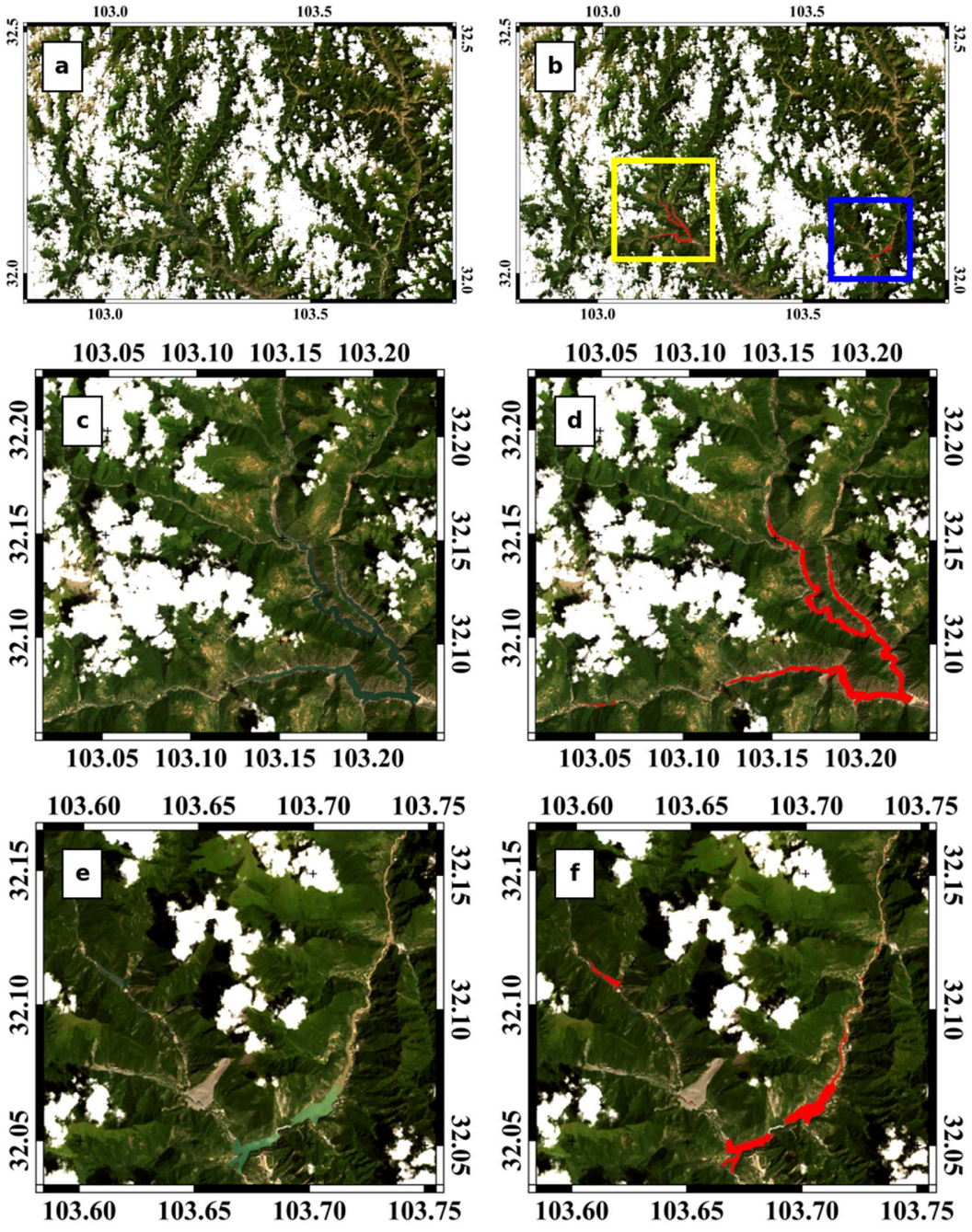

Fig. 12 (a) RGB image over a complex mountain area in the North West of China (15/08/2018). (b) Results of the WiPE algorithm with the detected water pixels appear in red. Each of the colored squares represent the two areas where water pixels have been detected. (c) RGB zoom on the region delimited by the yellow square. (d) Result of the WiPE algorithm on the region in (c). (e) and (f) as (c) and (d) but for the region delimited by the red square.

Being aware of these specific and complex situations, the performance and limitation of the WiPE algorithm are now addressed in details using the second data set gathering images collected by the OLI sensor over contrasted coastal and inland environments. For each selected image, a reference water pixels map (referred to as the reference WPM hereafter) was derived as follows. First the WiPE algorithm has been applied on the image. Then, based on a visual analysis of the image, polygons have been drawn using the QGIS software on the missing water pixels areas (P1) as well as on the areas where WiPE wrongly classify pixels as water pixels (P2). The reference WPM for each image is then generated using the results of WiPE corrected by adding (removing) water pixels from the P1 (P2) polygons. The Mean Absolute Percentage Difference (MAPD) is then calculated between the reference number of water pixels (WPM), and the number of water pixels generated by WiPE and Fmask (Table 2).

.

The evaluation of WiPE, and the inter-comparison with Fmask (version 3.3) have been performed over the whole validation data set (Table 2), but illustrations are only provided for some representative areas extracted from 6 different scenes and presenting a large range of complex situations (Fig. 13-18). For the 12 complete scenes used for the validation, the MAPD values range between 0.005 and 6% for WiPE. Over the six examined sub-scenes, the highest MAPD value of 11% was related to the presence of thin clouds. The MAPD present higher values for Fmask than for WiPE, with a general tendency for Fmask to under-estimate the number of water pixels, mainly in the presence of turbid waters. Note that for three of the twelve tested scenes, Fmask does not provide any possible solution. Similarly to Fmask, the distinction between water pixels and clouds, as well as between vegetation/land/barren land and water pixels are generally well performed by WiPE (Figs. 13-17). The main differences between the two algorithms are observed over very turbid waters (Figs. 13-14), cloud shadows over waters (Figs. 13, 15, 16, 17), and complex coastal environments (Fig. 18).

Table 2. Performance of the WiPE and Fmask algorithms on the validation data set. The number of water pixels identified by Fmask, WiPE, and “visual” interpretation (see text) are used to calculate the Mean

459 Absolute Percentage Difference (MAPD in %). The number are given for the whole 12 considered scenes,
460 while the number between brackets are those obtained over the 6 different sub-scenes provided in Figs.
461 13-18.

Figure N°	Fmask (water pixel)	WiPE (water pixel)	Visual interpretation	MAPD_Fmask (%)	MAPD_WiPE (%)
Name: LC80110622015137LGN00 Location: Rio Guayas, Ecuador					
13	11,761,455	12,525,625	12,400,369	5.15 (7.8)	1.01 (0.005)
Name: LC81180392015039LGN00 Location: Hangzhou Bay, China					
14	1,810,769	6,862,337	6,793,712	73.35 (87.74)	1.01 (0.006)
Name: LC82330542015220LGN00 Location: Rio Grande, Venezuela					
15	4,181,740	4,287,095	4,244,224	1.47 (14)	1.01 (11)
Name: LC80200242014261LGN00 Location: Moose River, Canada					
16	7,829,913	11,161,707	10,938,473	28.42 (24.6)	2.04 (0.04)
Name: LC81360452015293LGN00 Location: Meghna River Estuary, Bangladesh					
17	25,151,428	25,330,607	25,254,615	0.41 (12.3)	0.30 (0.005)
Name: LC81220442015291LGN00 Location: Zhujiang River, China					
18	4,824,260	4,247,824	4,162,868	15.89 (28.1)	2.04 (0.08)
Name: LC81230512016045LGN00 Location: Center East Sea, Vietnam					
	NA	28813483	27949071	NA	3.09
Name: LC81480452015153LGN00 Location: Gulf of Khambhat, India					
	1,872,122	5,436,606	5,408,972	65.39	0.51
Name: LC82040522015305LGN00 Location: Geba River Estuary, Guinea-Bissau					
	12,859,652	16,041,540	15,602,484	17.58	2.81
Name: LC82240842015061LGN00 Location: Rio de La Plata, Argentina-Uruguay					
	NA	11623842	12408451	NA	6.32
Name: LC82250602014321LGN00 Location: Rio Amazonas, Brazil					
	3,094,867	5,073,280	4,933,148	37.26	2.84
Name: LC81230522016045LGN00 Location: Center East Sea, Vietnam					
	NA	25,447,149	25,632,556	NA	0.72

462

463 The image acquired over the Rio Guayas (Fig. 13) shows that while the two approaches provide
464 relatively good results over most of the image (MAPD of 7.8% and 0.005% for Fmask and WiPE,
465 respectively), only WiPE is able to extract very turbid water pixels as those encountered far from the

466 river mouth (red circle n°2 in Fig. 13). From the river mouth to the upper part of the river, the maximum
467 value of the $\rho_{rc}(\lambda)$ spectrum, driven by the water leaving signal, shifts from the green (Fig. 13e) to the
468 near-infrared (Fig. 13f), a typical spectral behavior observed when the water turbidity increases (Han et
469 al., 2016). This pattern is observed over different scenes where the $\rho_{rc}(\lambda)$ spectra peak in the near-infrared,
470 as the one provided in Fig. 14 showing part of the Hangzhou bay where the Qiantang river, characterized
471 by high concentration of sediment, flows (Xie et al., 2013). For this specific image, almost all "true"
472 water pixels are detected as land pixels by Fmask (MAPD = 87.7%), and few of them, probably partly
473 due to the low temperature (5°C), as snow pixels (Fig. 14). In contrast, WiPE is able to identify properly
474 water pixels over the whole scene (MAPD=0.006%). The areas where turbid water pixels are falsely
475 identified as land by Fmask present a $\rho_{rc}(\lambda)$ spectrum with a maximum in the near-infrared (Fig. 14f).
476 The very few water pixels which are correctly detected by Fmask over this very turbid area are those for
477 which the maximum $\rho_{rc}(\lambda)$ values are reached in band 4 (see red circle n°1 in Fig. 14e) or band 3 as for
478 the water pixels in the bottom left corner of Fig. 14g. For low turbidity level, where the $\rho_{rc}(\lambda)$ maximum
479 values are not reached in the near-infrared (band 5), water pixels are generally well detected by the two
480 different algorithms (Fig. 13, 15-18). As mentioned by Zhu and Woodcock (2012), the adopted threshold
481 procedure for the detection of water bodies from Fmask works well for most water bodies but may fail
482 over cold (compared to surrounding areas) and bright (i.e. turbid) pixels. For this reason, and in a similar
483 way to the procedure applied for the detection of clouds in land areas, the last version of Fmask uses a
484 dynamic threshold for detecting clouds in water areas (Zhu et al. 2015). While such dynamical approach
485 provides better cloud detection over water areas (Zhu et al. 2015), the present study shows that detection
486 of water pixels over very turbid waters, where the maximum $\rho_{rc}(\lambda)$ value is observed at band 5, is still
487 not satisfactory. The dynamic threshold procedure used in Fmask should then be adapted for such
488 environments.

All images show that the detection of shadow pixels over water increases after the application of the HSV–space based criteria (i.e. the second step of WiPE). While some "true" shadow pixels are considered as water after the application of the first step of the algorithm (black circles in panels b of Figures 13, 14, 16, 17), they are correctly identified as shadow after the second step (black circles in panels c of Fig. 13, 14, 16, 17). The detection of thin clouds, especially over clear waters, seems to be slightly underestimated by WiPE (already discussed in section 3.2) and Fmask (see white circles Figure 13). Cloud masking is usually well performed by the two different approaches. However, while the new approach tends to slightly under-estimate the cloud shadow areas in favor of water pixels, Fmask tends to over-estimate cloud shadow areas. Cloud shadow pixels which are classified as water by the new approach are those belonging to the confusing area in the V-S space (Fig. 10). An example of wrong shadow pixel identification by WiPE is provided in Fig. 15 (black circles). These pixels, which are characterized by a $\rho_{rc}(\lambda)$ maximum in the red (channel 4), present V and S values around 0.12, and 0.26, respectively, and are therefore classify as belonging to the confusing space, for which a flag could be raised during the image processing. In the same way, Fmask, which provides relatively good estimates of cloud shadows, may falsely classify cloud shadows as water pixels, especially when the shadow area is located over land (Fig. 16) and barren land (Fig. 18). Over very complex areas such as the harbor area of the outlet of the Zhujiang river in China (Fig. 18) the new algorithm performs remarkably well. Fine structures like harbor protections in water are identified. Misclassification of construction as cloud by Fmask may also occur (the southern part of the image in Fig. 18), resulting in a detection of false shadow pixels over water areas.

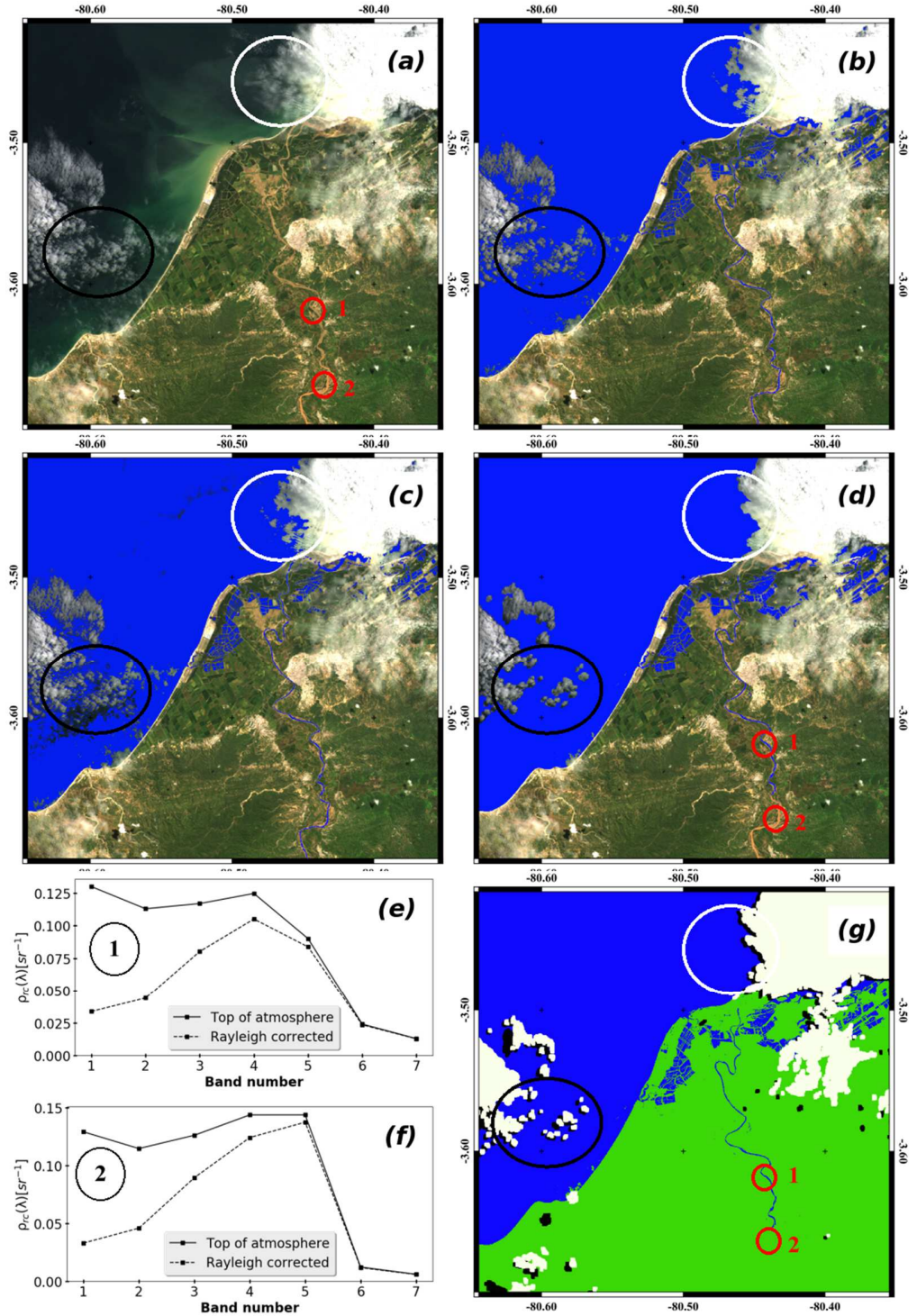

Fig. 13. (a) RGB image over the Rio Guayas (Ecuador, 17/05/2015). Results of the water pixel extraction (in blue) after the first (b) and second (c) steps of the new algorithm and of Fmask (d). (e and f) $\rho_{rc}(\lambda)$ spectra extracted over the two identified sub-pixels identified by red circles. (g) as (d) but showing the results of Fmask using a color code for water (blue), land (green), cloud (white), shadow (black), and

514 snow (yellow). Note that snow is not present in this image. The black and white circles show area of
515 cloud shadow and thin clouds (see text).

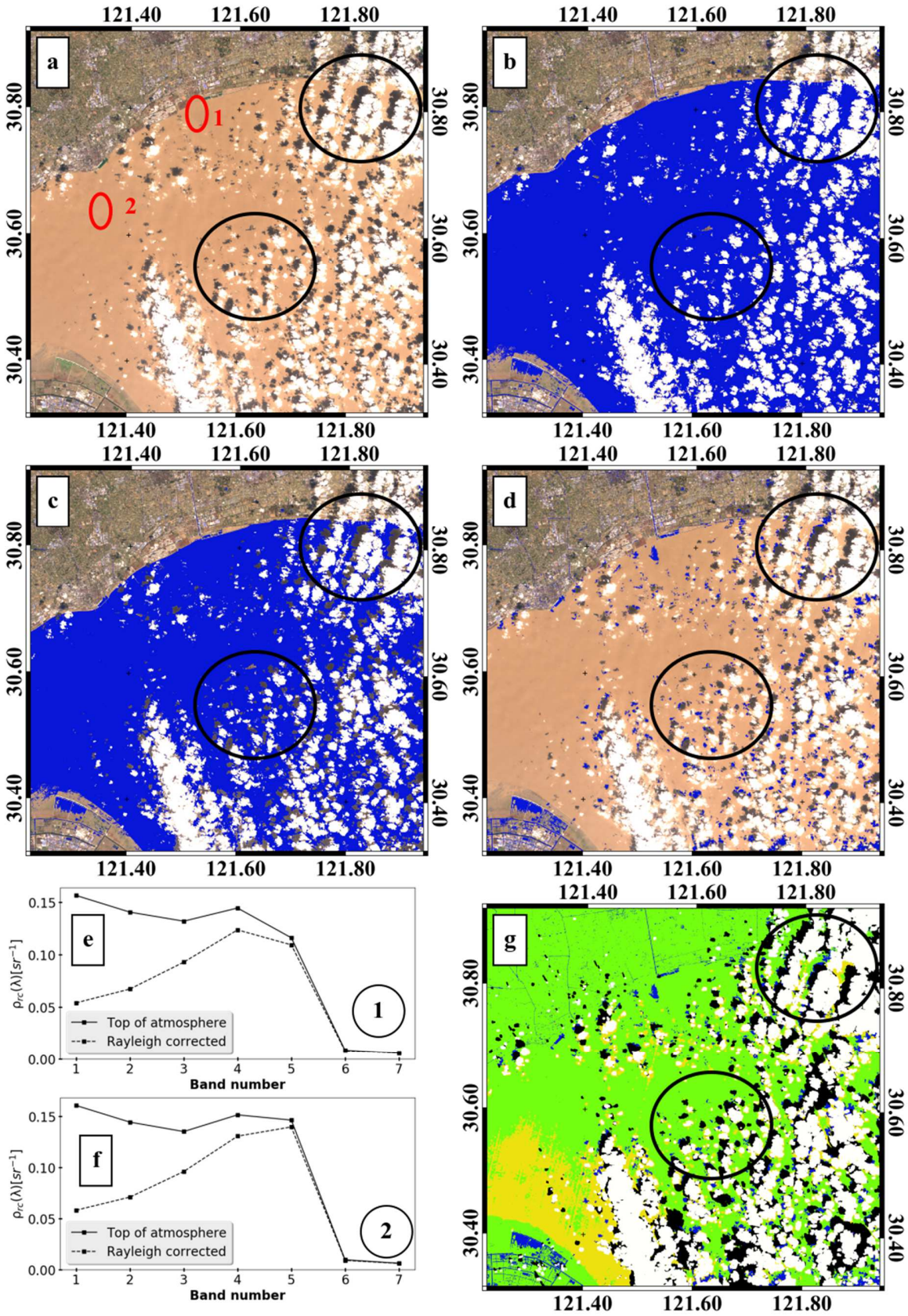

516

517 **Fig. 14.** As Fig. 13 but for the Hangzhou bay (China, 08/02/2015).

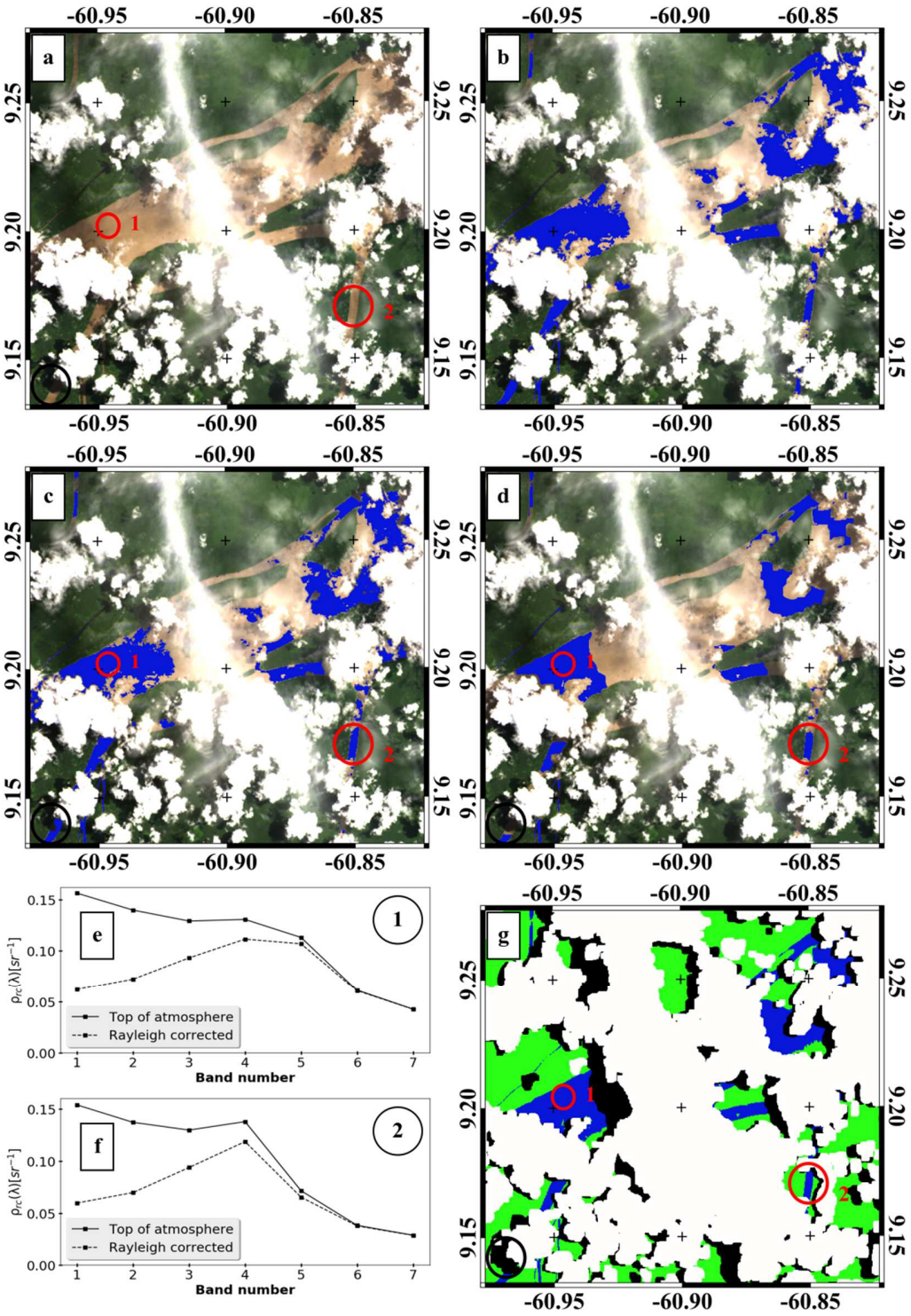

518

519 **Fig. 15.** As Fig. 13 but for the Rio Grande (Venezuela, 17/11/2014)

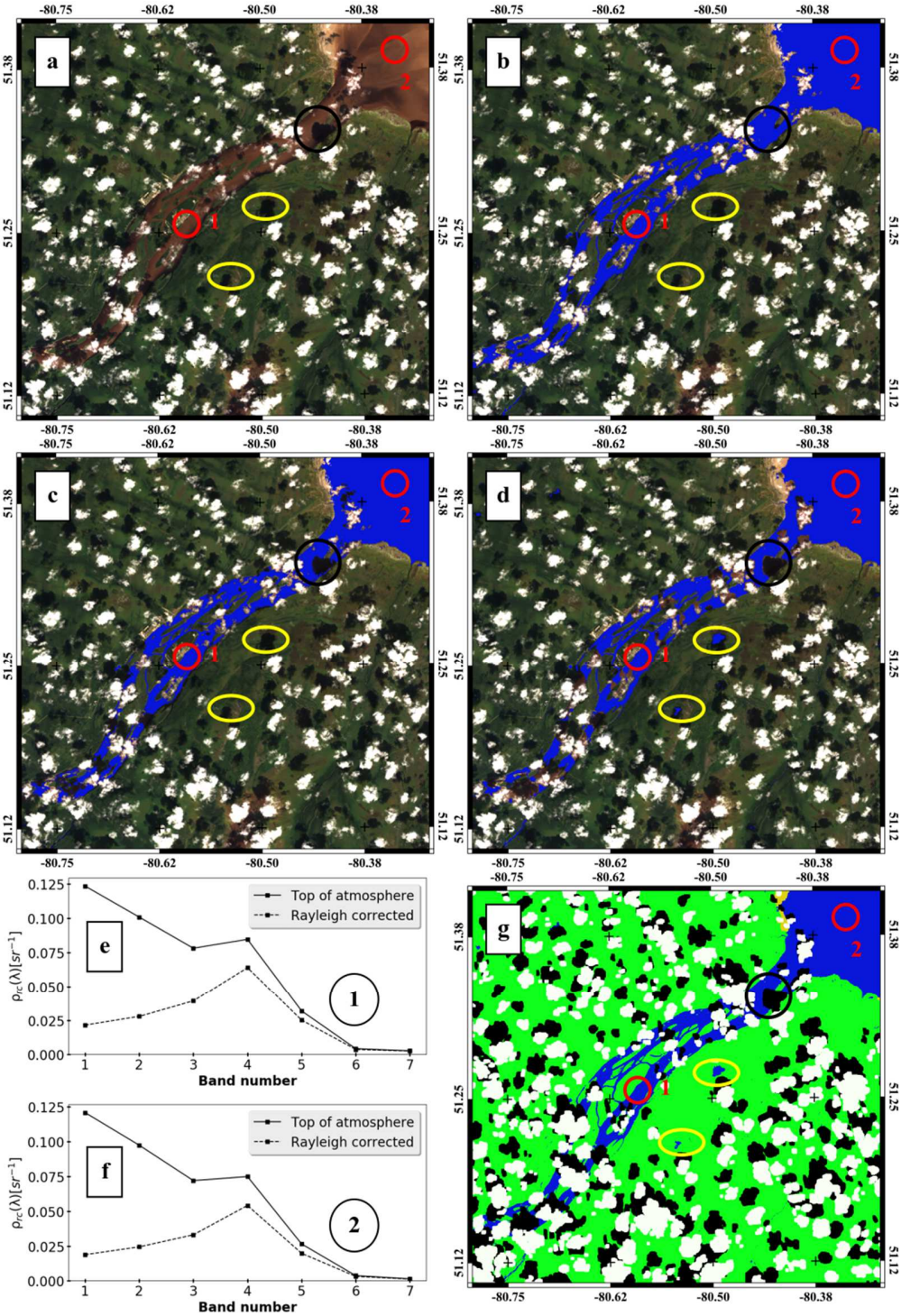

520

521 **Fig. 16.** As Fig. 13 but for the Moose river (Canada, 18/09/2014). The yellow circles show land areas

522 identified as water by Fmask, the black circle shows a cloud shadow area, and red circles delimit the

523 water areas where the $\rho_{rc}(\lambda)$ spectra 1 (e) and 2 (f) are extracted (see text).

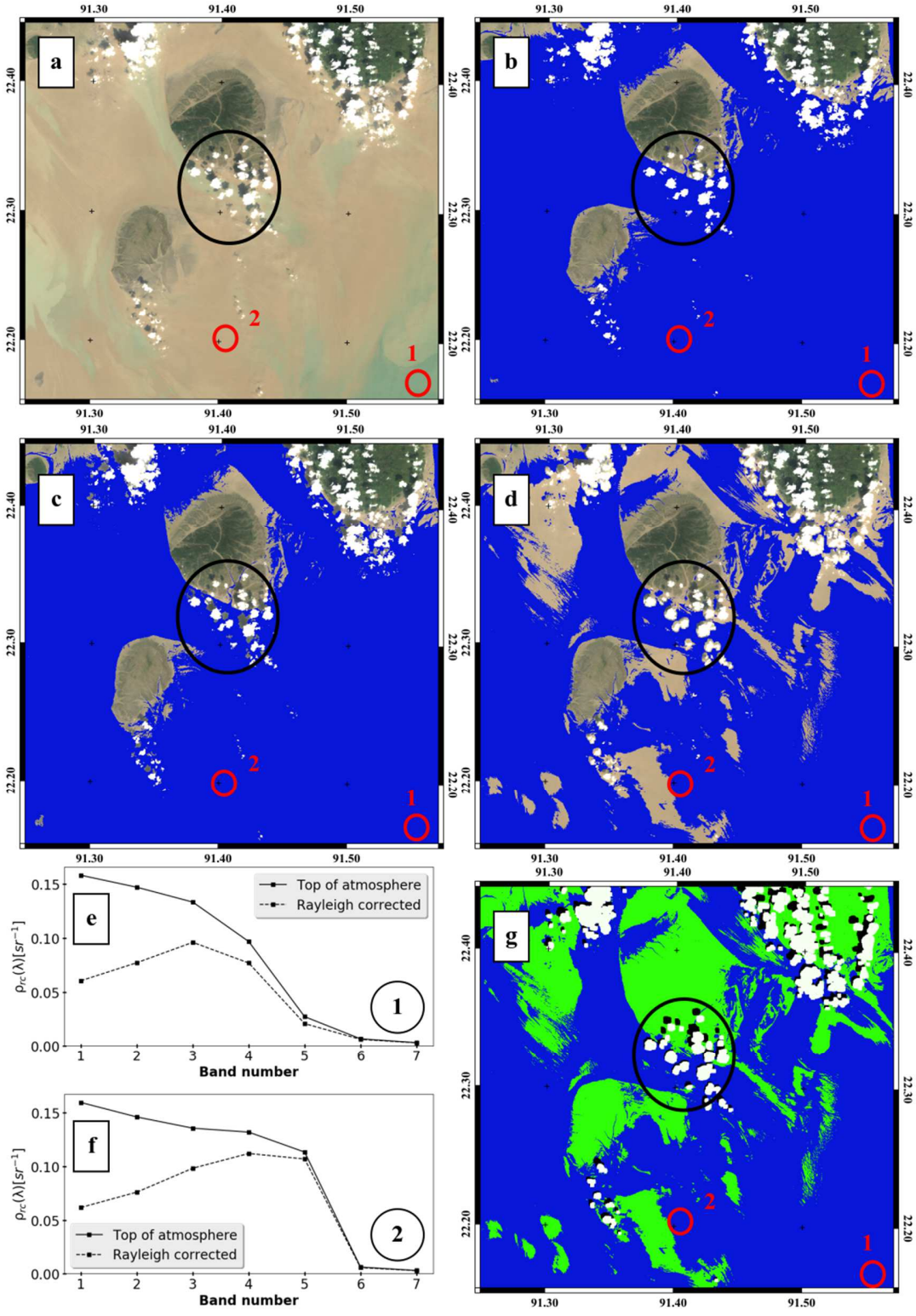

524

525 **Fig. 17**. As Fig. 13 but for the Maghna estuary (Bangladesh, 20/10/2015)

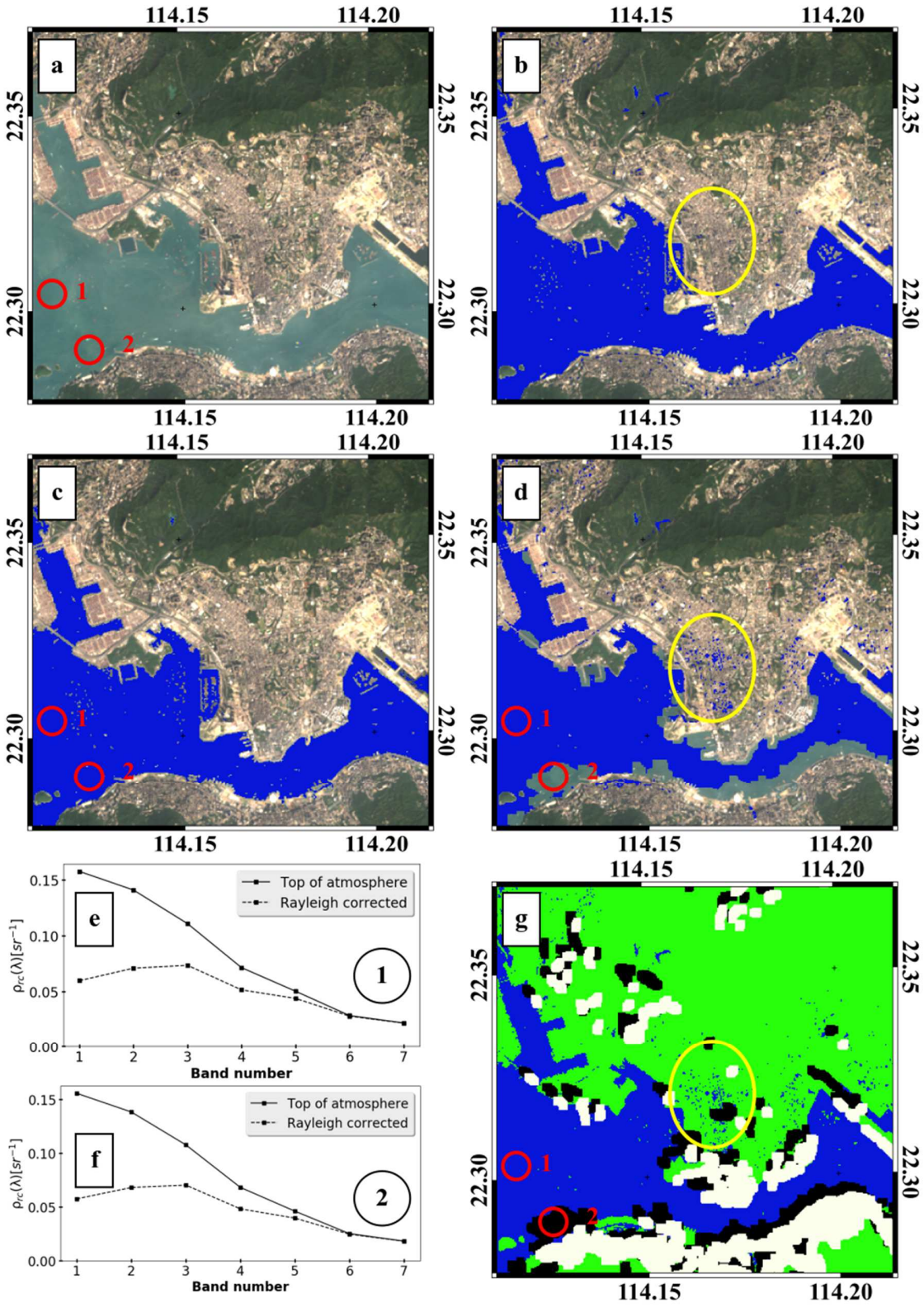

Fig. 18. As Fig. 13 but for the Hong Kong bay (China, 18/10/2015).

5. Adaptation of WiPE for MSI on Sentinel 2a

The WiPE algorithm, originally developed for L8-OLI, has been adapted to S2a-MSI using the seven following spectral bands: bands 2 (496.6 nm), 3 (560 nm), 4 (664.5 nm), 7 (782.5 nm), 10 (1373.5 nm), 11 (1613.7 nm), and 12 (2202.4 nm). The same methodology used to develop WiPE for L8-OLI, has been adopted for S2a-MSI. The two steps are both applied to the Rayleigh corrected reflectance. The first step is dedicated to the removal of barren land, construction, vegetation, clouds and a minority of thin clouds and clouds shadows. The second step, based on the HSV transformation, is dedicated to the removal of the remaining thin clouds and cloud shadows. Similar results as those obtained for L8-OLI have been obtained in terms of water pixel extraction, as demonstrated by the complex image of an aquaculture area in the Huangmao river estuary in China (Fig. 20) or over the Tonle Sap in Cambodia (Fig. 21). It is worth to notice that, thanks to the high spatial resolution of MSI, fish cages present in the Huangmao river estuary illustration map are well detected and not mixed with water pixels (Fig. 20d).

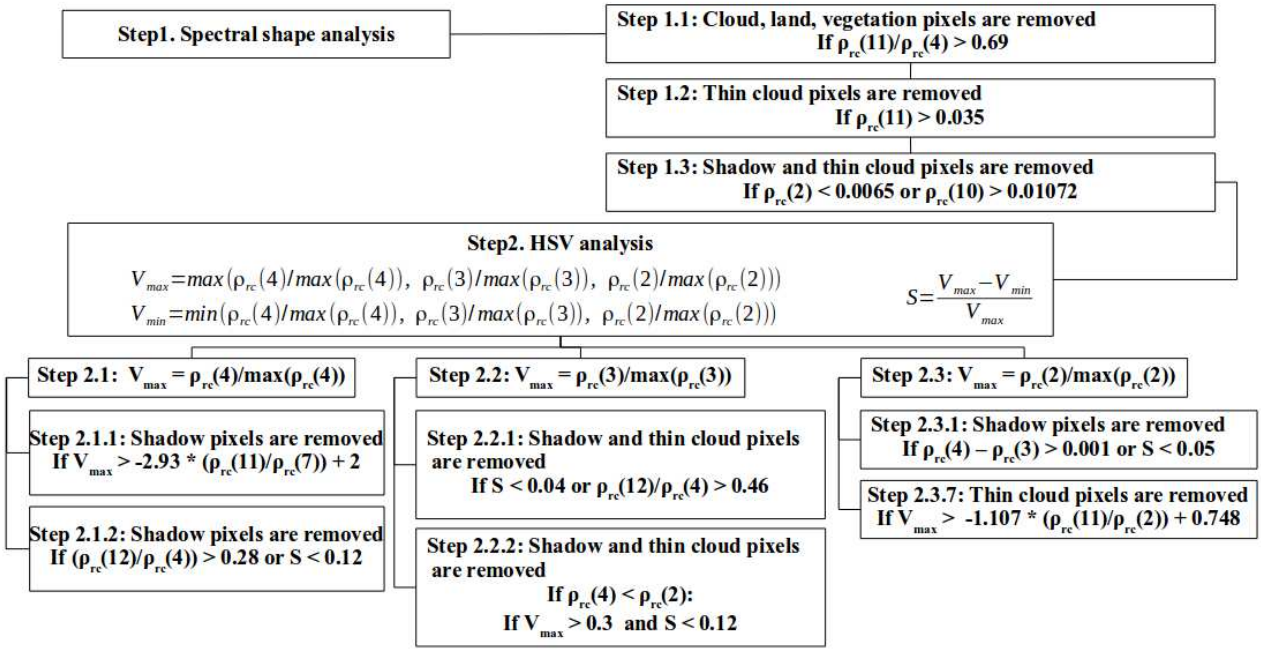

Fig. 19. The logic flow of the water extraction pixel algorithm based on the combination of spectral shape analysis (step 1) and HSV analysis (step 2) for the S2a-MSI sensor. This flowchart requires the Rayleigh corrected reflectance (Eq.11) at bands 2, 3, 4, 7, 10, 11, and 12 as input parameters.

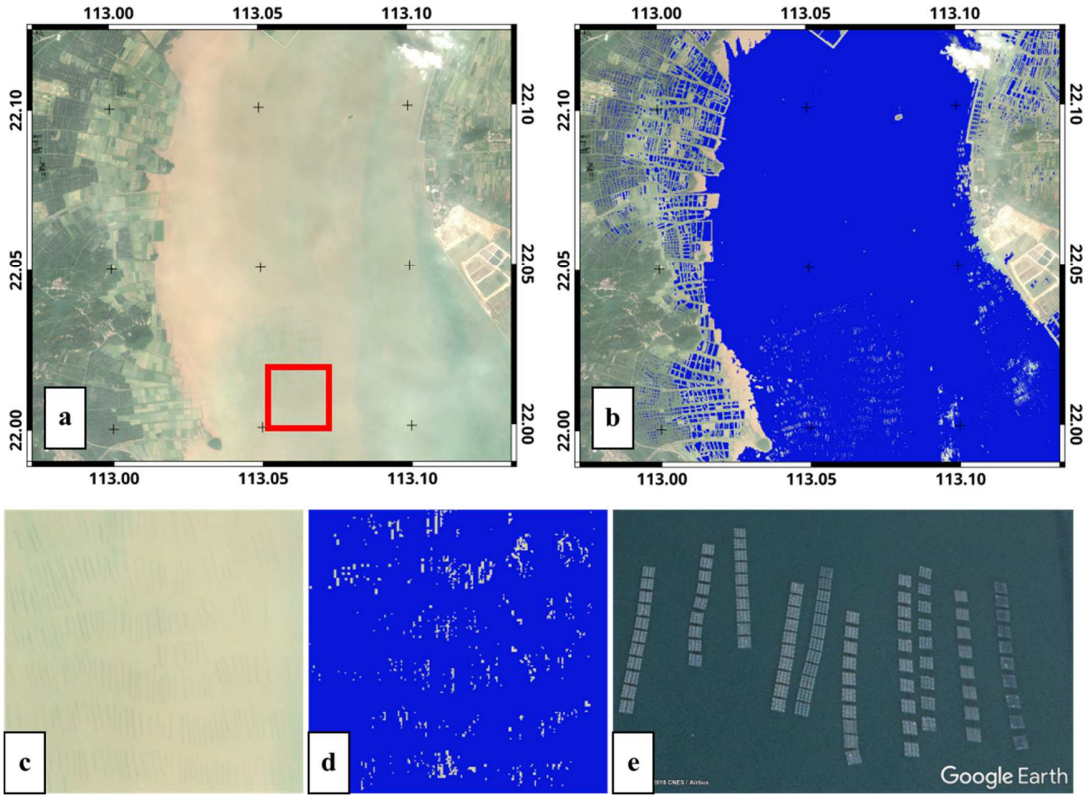

Fig. 20. (a) RGB image over the Huangmao river estuary in China. (b) Results of the water pixel extraction by WiPE. (c) Zoom of the area framed in red (a) showing the fish cages which are also identified with WiPE in (b) and zoomed in (d). (e) Fishes cages showed from Google Earth image.

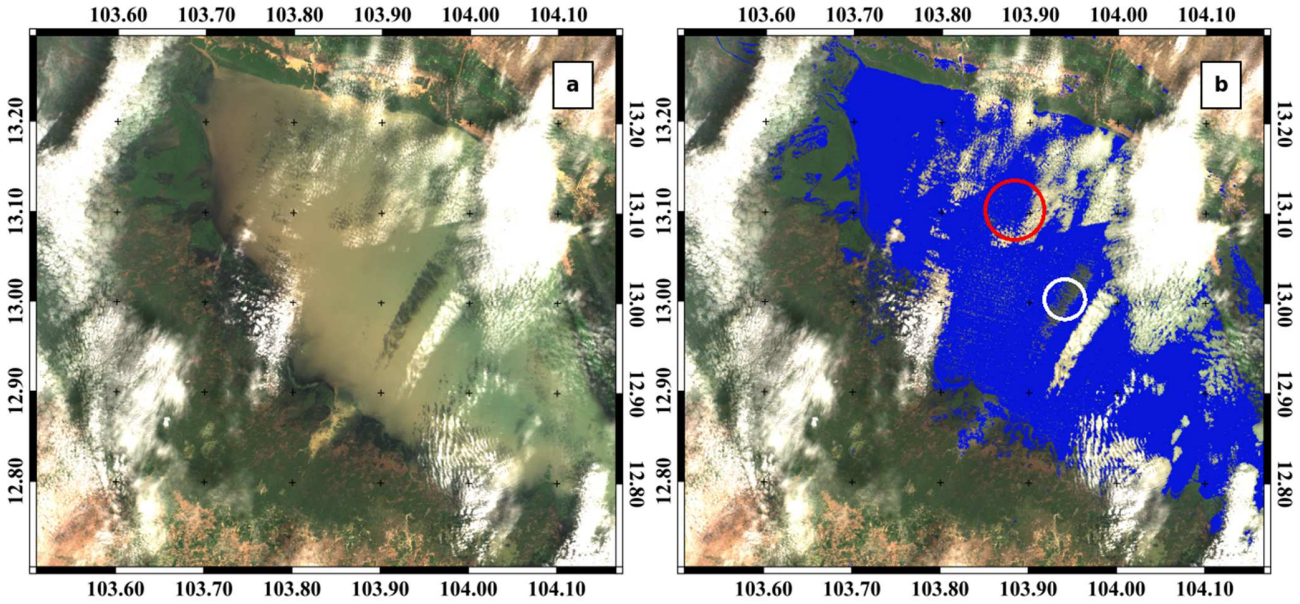

558

559 **Fig. 21.** (a) RGB image over the Tonle Sap in Cambodia. (b) Results of the water pixel extraction by
560 WiPE. The white and red circles indicate situations with correct and wrong cloud shadows identification,
561 respectively.

562

563 In contrast to L8-OLI for which the spatial resolution of all bands is the same and equal to 30
564 meters, the spatial resolution of the algorithm-required bands for S2a-MSI are equal to 10 (bands 2, 3,
565 and 4), 20 (7, 11, and 12), and 60 (band 10) meters. These different spatial resolutions introduce some
566 artefacts in the extraction of water pixels, especially at the border of objects under strong contrast, such
567 as cloud shadow in the immediate proximity of clouds. This is clearly illustrated in Fig. 21 where cloud
568 shadows are well detected when they are relatively far from the cloud (white circle in Fig. 21b), and not
569 detected when they are at the very border of the clouds (red circle in Fig. 21b). Future works are therefore
570 needed to figure this specific issue out.

571

572 **6. Concluding remarks**

573 Remote sensing is a major observation tool for estimating surface water areas for many
574 environmental and economical applications (aquaculture, flooding survey, water management, etc). In
575 addition to this quantification aspect of surface water bodies, the detection of water pixels from remote
576 sensing observations is an essential and critical step before the application of adapted algorithms aiming
577 at estimating parameters describing the biogeochemical status of surface water bodies from space. A new
578 algorithm (referred as WiPE) has been developed to assess water pixels from L8-OLI, and has been
579 adapted for the MSI sensor. Unlike existing algorithm, WiPE is based on the Rayleigh-corrected
580 reflectance, $\rho_{rc}(\lambda)$, which makes it more sensitive to the spectral signature of the different objects
581 considered: clouds, thin clouds, cloud shadow, vegetation, barren land, construction, and water. In
582 contrast to other approaches, such as Fmask, the present algorithm is not able to distinguish the different
583 considered objects individually, but rather to extract water pixels from other pixels. For that purpose, this
584 algorithm consists of two main steps. First, clouds, thin clouds over land, cloud shadow over land,
585 vegetation, barren land, and construction are removed based on a spectral shape analysis of $\rho_{rc}(\lambda)$.
586 Second, the Rayleigh-corrected reflectance spectra are transferred into the HSV color space to improve
587 the distinction between water pixels and thin cloud and shadow pixels over water areas not affected by
588 sun glint. This second step is based on the contrast of the whole image, and does not require any
589 knowledge on the position and altitude of clouds. The present algorithm generally shows very good
590 performance for the detection of water pixels over complex aquatic environments, especially in very
591 turbid areas where the maximum of $\rho_{rc}(\lambda)$ is observed in the near-infrared. The main limitation of the
592 approach is for the detection of cloud shadow over blue to green waters where a confusion between cloud
593 shadow pixels and water pixels may occur. As WiPE does not make any assumption on the
594 presence/absence of clouds and then on the potential location of areas affected by cloud shadow, future
595 improvement of the method could account for the proximity of clouds.
596

6. Acknowledgment

This research has been supported by the University of Science and Technology of Hanoi (USTH) in the frame of the VIETNAMINs project and by the ESRIN Contract 4000115822/15/I-SBo – "Scientific Exploitation of Operational Missions (SEOM) S2-4Sci Land and Water Atmospheric corrections for coastal and inland waters. This work has also beneficiated from the support of VAST.HTQT.NGA.15-07/16-17 for data processing and the funding of the CNES TOSCA HARDECOT project. We thank the associate editor, Frédéric Mélin, and three anonymous reviewers for their constructive comments on the manuscript.

7. References

Concha, J. A., Schott, J. R., 2016. Retrieval of color producing agents in Case 2 waters using Landsat 8. Remote sensing of Environment. 185, 95-107.

Franz, B.A., Bailey, S.W., Kuring, N., Werdell, P.J., 2015. Ocean color measurements with the Operational Land Imager on Landsat-8: implementation and evaluation in SeaDAS. Journal of Applied Remote Sensing. 9, 096070, 1-16.

Ganesan, P., Rajini, V., Sathish, B.S, Shaik, K.B., 2014. HSV color space based segmentation of region of interest in satellite images. International Conference on Control, Instrumentation, Communication and Computational Technologies. 101-105.

Gordon, H. R., 1997. Atmospheric correction of ocean color imagery in the Earth Observing System era. Journal of Geophysical Research. 102, 17081-17106.

Gordon, H. R., Brown, J. W., Evans, R. H., 1988. Exact Rayleigh scattering calculations for use with the Nimbus-7 coastal zone color scanner. Applied Optics. 27, 862-871.

619 Han, B., Loisel, H., Vantrepotte, V., Mériaux, X., Bryère, P., Ouillon, S., Dessailly, D., Xing, Q., Zhu,
620 J., 2016. Development of a Semi-Analytical Algorithm for the Retrieval of Suspended Particulate
621 Matter from Remote Sensing over Clear to Very Turbid Waters. *Remote Sensing*. *8*, 211, 1-23.
622 Xu, H., 2006. Modification of Normalized Difference Water Index (NDWI) to Enhance Open Water
623 Features in Remotely Sensed Imagery. International Journal of Remote Sensing. 27, 14, 3025-
624 3033.
625 Jawak, S. D., Kulkarni, K., Luis, A. J., 2015. A review on extraction of lakes from remotely sensed
626 optical satellite data with a special focus on cryospheric lakes. Advances in Remote Sensing, 4,
627 196–213.
628 Kartar, S., Mili, G., Shubha, S., 2015. WSB-DA: Water Surface Boundary Detection Algorithm Using
629 Landsat 8 OLI Data. IEEE Journal of Selected Topics in Applied Earth Observations and Remote
630 Sensing. 9. 363-368.
631 Lee, Z., Shang, S., Qi, L., Yan, J., Lin, G., 2016. A semi-analytical scheme to estimate Secchi-disk
632 depth from Landsat-8 measurements. Remote Sensing of Environment. 177, 101-106.
633 Li, Y., Zhang, Y., Shi, K., Zhou, Y., Zhang, Y., Liu, X., Guo, Y., 2017. Spatiotemporal dynamics of
634 chlorophyll-a in a large reservoir as derived from Landsat 8 OLI data: understanding its driving
635 and restrictive factors. *Environmental Science and Pollution Research*. ISSN 0944-1344.
636 Lymburner, L., Botha, E., Hestir, E., Anstee, J., Sagar, S., Dekker, A., Malthus, T., 2016. Landsat 8:
637 Providing continuity and increased precision for measuring multi-decadal time series of total
638 suspended matter. Remote Sensing of Environment. 185, 108-118.
639 McFeeters. S.K., 1996.The use of the Normalized Difference Water Index (NDWI) in the delineation
640 of open water features. International Journal of Remote Sensing. 17, 1425-1432.
641 McFeeters, S.K., 2013. Using the Normalized Difference Water Index (NDWI) within a Geographic
642 Information System to Detect Swimming Pools for Mosquito Abatement: A Practical Approach.
643 *Remote Sensing*. *5*, 3544-3561.

644 Nordkvist, K., Loisel, H., Gaurier, L. D., 2009. Cloud masking of SeaWiFS images over coastal waters
645 using spectral variability. Optics Express. 17, 12246-12258.
646 Pahlevan, N., Schott, J. R., 2013. Leveraging EO-1 to evaluate capability of new generation of Landsat
647 sensors for coastal/inland water studies. IEEE Journal of Selected Topics in Applied Earth
648 Observations and Remote Sensing. 6, 360-374.
649 Pahlevan, N., Schott, J.R., Franz, B.A., Zibordi, G., Markham, B., Bailey, S., Schaaf, C.B., Ondrusek,
650 S.G., Strait, C.M., 2017. Landsat 8 Remote Sensing Reflectance (Rrs) Products, Evaluations,
651 Intercomparisons, and Enhancements. Remote Sensing of Environment. 190, 289-301.
652 Pratt, W.K., 2001. Digital Image Processing, third ed. Wiley, New York, USA.
653 Pekel, J.F., Vancutsem, C., Bastin, L., Clerici, M., Vanbogaert, E., Bartholomé, E., Defourny, P.,
654 2014. A near real-time water surface detection method based on HSV transformation of MODIS
655 multi-Spectral time series data. Remote Sensing of Environment. 140, 704-716.
656 Rouse, W., Haas, R. H., Schell, J. A., Deering, D. W., 1973. Monitoring Vegetation Systems in the
657 Great Plains with ERTS. Proceedings of the 3rd ERTS Symposium. 1, 309-317.
658 Shen, X., Li, Q., Tian, Y, Shen, L., 2015. An Uneven Illumination Correction Algorithm for Optical
659 Remote Sensing Images Covered with Thin Clouds. Remote Sensing. 7, 11848-11862.
660 *Slonecker, E. T., Daniel, K. J., Brian, A. P., 2016*. The new Landsat 8 potential for remote sensing of
661 colored dissolved organic matter (CDOM). Marine Pollution Bulletin. 107, 518-527.
662 Smith, A., 1978. "Colour Gamut Transform Pairs," SIGGRAPH 78 Conference Proceedings, 12–19.
663 Reprinted in Tutorial: Computer Graphics, 1982, edited by J. C. Beatty and K. S. Booth, IEEE
664 Computer Society Press, Silver Spring, MD, 2nd edition, 376–383.
665 Tiit, K., Casal, P.G., Claudio, B., Birgot, P., Renato, F., Lino, C., Kaire, T., 2016. Mapping inland
666 water carbon content with Landsat 8 data. International Journal of Remote Sensing, 37, 13, 2950-
667 2961.

668 Urbanski, J.A., Wochna, A., Bubak, I., Grzybowski, W., Lukawska-Matuszewska, K., Łącka, M.,
669 Śliwińska, S., Wojtasiewicz, B., Zajączkowski, M., 2016. Application of Landsat 8 imagery to
670 regional-scale assessment of lake water quality. International Journal of Applied Earth
671 Observation and Geoinformation. 51, 28-36.
672 Vanhellemont Q., Ruddick K., 2014. Turbid wakes associated with offshore wind turbines observed
673 with Landsat 8. Remote Sensing of Environment. 145, 105-115.
674 Vermote, E. F., Saleous, N. Z., 2006. Operational atmospheric correction of MODIS visible to middle
675 infrared land surface data in the case of an infinite Lambertian target. Earth Science Satellite
676 Remote Sensing, Science and Instruments. 1, 123–153. Edited by J. J. Qu et al.. Tsinghua Univ.
677 Press, Beijing.
678 Wang, M., Bailey, S. W., 2001. Correction of sun glint contamination on the SeaWiFS ocean and
679 atmosphere-products. Applied Optics. 40, 4790-4798.
680 Wang, M., Michael, D.K., 1997. Correction of Rayleigh scattering effects in cloud optical thickness
681 retrievals. Journal of Geophysical Research. 102, 25915-25926.
682 Xie, D.F., Gao, S., Wang, Z., Pan, C., 2013. Numerical modeling of tidal currents, sediment transport
683 and morphological evolution in Hangzhou Bay, China. International Journal of Sediment
684 Research. 28, 3, 316-328.
685 Zhu, Z., Woodcock, C. E., 2012. Object-based cloud and cloud shadow detection in Landsat imagery.
686 Remote Sensing of Environment. 118, 83-94.
687 Zhu, Z., Wang, S., Woodcock, C. E., 2015. Improvement and expansion of the Fmask algorithm:
688 cloud, cloud shadow, and snow detection for Landsats 4-7, 8, and Sentinel-2 images. Remote
689 Sensing of Environment. 159, 269-277.